Searching for the Signature of a Tetraneutron Resonance

by

Conor Waterfield

A THESIS SUBMITTED IN PARTIAL FULFILMENT OF
THE REQUIREMENTS FOR THE DEGREE OF

BACHELOR OF SCIENCE

in

Honours Astrophysics

(Department of Astronomy and Physics, Dr. Rituparna Kanungo supervising faculty)

.....

.....

.....

.....

.....

SAINT MARY'S UNIVERSITY

April 21, 2021

Abstract

Searching for the Signature of a Tetraneutron Resonance

by *Conor Waterfield*

submitted on April 21, 2021:

Many environments in the universe give rise to conditions extreme enough to allow exotic forms of nuclear matter. Understanding how this matter interacts allows us to better understand the nuclear forces and astronomical phenomena such as neutron stars. A tetraneutron is an exotic nuclear form which is composed of four neutrons. Its existence is debated, with an open question whether they can be held together briefly in a short-lived resonant state. The existence of the tetraneutron state would be observable in reactions with four neutrons as their end product. At the IRIS facility at TRIUMF, an experiment involving the reaction $^{8}He(d,^{6}Li)4n$ was carried out by reacting a beam of ^{8}He with a deuterium target and measuring the kinematics of the resulting ^{6}Li. The existence of the tetraneutron state could be determined from the missing mass spectrum. In order to be able to interpret the results of the experiment, the effect of the non-resonant four neutron final state must be determined. This is done by simulating the non-resonant reaction with five-body final state through the experimental setup. This thesis covers my work in building this simulation using the properties of the reaction and the experimental setup.

Contents

List of Figures

List of Tables

Chapter 1

Introduction

Over the course of the last century, our understanding of nuclear physics has allowed us to better understand the structure of the visible matter around us. Understanding the forces that hold together nuclei can give us insight into the structures they can form and can be applied to new technologies and our understanding of astrophysical phenomena. In this work, we will search for the signature of one such structure, a tetraneutron resonance, through a transfer reaction experiment performed using the ISAC Charged Particle Reaction Spectroscopy Station (IRIS) facility at TRIUMF in Vancouver, BC.

1.1 Bound States and Resonances

1.1.1 Bound States

In nuclear physics, there are several states of stability for subatomic systems. The more familiar isotopes, ^{4}He, ^{12}C, ^{16}O, etc. are examples of stable systems; they do not decay and last for long timescales. These isotopes are bound, they are a collection of nucleons that remain together due to an attractive nuclear force. Beyond these, there are unstable isotopes, such as ^{8}He, ^{14}C and ^{235}U. These isotopes are still bound, they are held together by the nuclear forces, but they are not energetically favorable.

After a certain amount of time, be it on the order of milliseconds or millenia, they will spontaneously decay into a more energetically favorable species.

Unbound systems, such as ^{9}He, ^{23}C and potentially the tetraneutron, are unable to form bound states; they can never hold themselves together and decay immediately - within around 10^{-20} seconds - by emitting nucleons, referred to as 'dripping'. These examples in particular are isotopes beyond the neutron drip line. The proton and neutron drip lines are the boundaries for where bound nuclei can exist. If a neutron is added to an isotope on the neutron drip line, it will not be bound in the system, and similarly for protons at the proton drip line. The proton drip line has a very clear culprit - the Coulomb force, which causes a repulsive force between the protons. The inter-nucleon nuclear force is simply not strong enough to counter the Coulomb force when there is an abundance of protons in the nucleus compared to the number of neutrons. Therefore, the stability of nuclei with more protons can only be maintained by also increasing the number of neutrons in order for the nuclear forces between the protons and neutrons to overcome the Coulomb repulsion.

The neutron drip line, on the other hand, gives rise to many more interesting phenomena. (1) There is no Coulomb force to push apart the neutral neutrons like there is for protons. Naively, one may expect that a nucleus could hold arbitrarily many neutrons, and while heavier nuclei do indeed skew towards having significantly more neutrons than protons, the neutron drip line still appears to exist. More neutron-rich isotopes of the same element will have smaller neutron separation energies, meaning

that there is a diminishing return when binding more neutrons, until the incremental binding energy goes to zero. This demonstrates that the forces keeping nuclei together are reliant on the proton-neutron attractive force to hold themselves, without any neutron-neutron attraction.

1.1.2 Resonances

Unbound systems last for a very short time before breaking apart. They can however have resonances, where they can be 'quasi-bound' for a very short time. Resonant states have energies, like the energy of bound states. These energies are part of the continuum at positive energy, as opposed to bound states at negative energy. As they are very short lived, the uncertainty principle means that there is a relationship between the lifetime of the state and its energy width. Resonances will show up as peaks at certain energies with a certain width. The nature of resonances will be discussed further in the section on theoretical approaches to searching for the tetraneutron resonance.

While the nature of resonances may seem unclear, their presence in nuclear physics phenomena make their importance apparent. A prime example of this is the Hoyle state, a resonance formed by ^{8}Be and ^{4}He, derived from its necessity to allow the triple alpha process to work. (2) The triple alpha process produces ^{12}C, which is required for the CNO cycle in heavy stars. Carbon is also a fundamental element in the formation of life, and as such, its abundance must be explainable by nucleosynthesis. It was apparent that the triple alpha was the best way to explain the abundances,

but the short lifetime of ^{8}Be meant that there should be no way for the formation of ^{12}C to happen fast enough to outpace the formation of heavier elements formed out of carbon and leave behind any amount of carbon. Hoyle made that prediction that there was a resonant state of ^{8}Be and ^{4}He with a resonance energy of approximately 0.31 MeV, which would put it at the level of an excited state of ^{12}C. Given the right width for the resonance, this was found to be able to give the known abundance of ^{12}C.

1.2 Tetraneutrons

1.2.1 Tetraneutrons

Given the behavior of nuclei near the neutron drip line, it could be asked what happens in the extreme circumstance where there are no protons at all. Dineutrons are the simplest example of such a system, though theoretical and experimental research has largely ruled them out. (3) Is it then possible to form resonances, or potentially even bound states, of higher numbers of neutrons? Trineutrons and tetraneutrons have both been studied extensively, but tetraneutron resonances are the most promising candidate.

The tetraneutron resonance would involve four neutrons coming together into a resonant state for a short time, and could be observed in principle in reactions with four neutrons as products. It is thought that in certain nuclei with four neutrons in halo structures outside of a stable core could form resonant structures. Through

collisions, the core could be stripped away, leaving the tetraneutron resonance, which would soon fall apart into the constituent neutrons. Evidence of this would be evident in the kinematics of the other reaction product.

1.2.2 Motivation

Finding evidence for tetraneutrons and understanding the forces that hold them together could be important in several areas in nuclear physics and astrophysics. As covered in the section on theory, there are a broad range of predictions for the tetraneutron resonance. On one end, it is shown that modern hamiltonians do not predict tetraneutrons. (4) Other predictions require the introduction of new physics such as strong three-body forces, neither of which would be consistent with our current understanding of nuclear forces. (5) There are, however, predictions from ab initio theory that do predict the possibility of resonant tetraneutrons with no changes to the current understanding of nuclear forces and would therefore make it consistent with other observations. (6) This could also potentially signify the utility of ab initio approaches over other theoretical approaches, should the tetraneutron resonance be found. More detail of these theoretical methods will be discussed in the section on theory.

Another area related to the tetraneutron resonance is that of neutron stars. In neutron stars, matter is compressed to high densities, and protons are converted to neutrons through electron capture. This dense, neutron-rich environment could give rise to conditions that facilitated the formation of tetraneutron resonances. Much like

tetraneutron resonances are predicted to be able to exist in the strong field holding halo neutrons, so too may they exist in the strong fields inside this environment. (7) If the tetraneutron resonance existed, it would therefore be expected to show up in neutron stars and potentially influence their observable properties. It was demonstrated by Ivanytskyi et al. that the presence of the resonance could lead to a more energetically favorable state in the material where some fraction of the neutrons are in tetraneutrons. This was found to be restricted to lower densities, though these densities could be found in the crust of the neutron star and potentially affect the microscopic properties. Understanding the nature of the tetraneutron resonance would be a useful tool in understanding this matter, and help to make better predictions of the properties of neutron stars.

1.3 Experimental Searches

Given the questions posed by the potential of the existence of tetraneutrons, experimental searches would be helpful in answering them. There have been many experiments attempting to find them, though up to this point, there have been only two experiments claiming to have detected Tetraneutrons, with many more showing no evidence. Many of these experiments have involved pions, such as ${}^4He(\gamma, 2\pi^+)4n$, ${}^4He(\pi^-, \pi^+)4n$ and ${}^7Li(\pi^-, {}^4He)4n$, (8) and more involved only nuclei, such as ${}^7Li({}^7Li, {}^{10}C)4n$. (9) The lack of evidence from these experiments demonstrate that the cross-sections for tetraneutrons from these reactions were too low to measure. There are some potential explanations for why these reactions were unable to yield tetraneutrons, as

opposed to those that claim to have found such evidence. These will be important to contrast with the two experiments that claim experimental evidence for tetraneutrons.

1.3.1 GANIL Experiment

In 2001, an experiment at GANIL claimed the detection of neutron clusters using a technique involving the breakup of neutron-rich nuclei. (10) The results claim six multi neutron cluster events from the channel of ^{14}Be breakup into $^{10}Be + 4n$, which would indicate a Tetraneutron. This experiment was the first to claim a detection of a Tetraneutron, which if affirmed would have the potential for discovery. The experiment included many potential sources of background which could explain these results, as well as some assumptions which may not be reliable enough to use as evidence for the claimed observations.

The experiment involved directing intermediate-energy (35A MeV) ions of ^{11}Li, ^{14}Be and ^{15}B into a carbon breakup target. The ion goes through two parallel-plate avalanche counters which measure the position the beam passes through them, then into a thin silicon detector which identifies the particle passing through. After this, there is a $275\,mg/cm^2$ carbon target which causes a breakup of the beam particle, fragmenting it into constituent parts. After this, there is a position-sensitive telescope made of silicon and cesium-iodide. Lastly, downstream from the telescope, there is a neutron detector called DEMON that derives the energy of neutrons freed in the reaction from time-of-flight.

The analysis of this data involved pulse-shape discrimination to eliminate contributions from gamma rays and cosmic rays, as well as quantifying energy deposited into protons in the DEMON detector. The detector measures energy in terms of not only the time-of-flight but also the recoil energy of protons, which are assumed to be less the energy of the neutron. In an ideal detector, the proton energy would never exceed the energy derived from time-of-flight, though in DEMON the limit is actually given as 1.4 for single-neutron detections. This is expected to be exceeded in the case of neutron clusters because the time-of-flight will be reduced due to the extra mass, while the energy given to the proton would still be measured correctly. Multi-neutron clusters are then identified based on whether they exceed this limit.

This analysis revealed seven counts exceeding the limiting energy ratio coming from the breakup of ^{14}Be, as shown in Figure 1.1. These counts all seemed to correlate with the detection of ^{10}Be from the breakup. There were also events found in the breakup of ^{11}Li, however, they did not appear to correlate with an individual expected breakup product as in the case of ^{14}Be into ^{10}Be. The correlation of each of the counts from ^{14}Be with the expected breakup product given the detection of tetraneutrons raised a lot of interest in this result as a potential for tetraneutron discovery. One of the counts appeared to correlate with a low-energy ^{10}Be detection in the cesium-iodide detector, which would be inconsistent with the expected kinematics if this were a neutron cluster reaction. The remaining six counts, however, were apparently consistent with being tetraneutron counts from the breakup reaction into ^{10}Be. The angles between the detected neutron clusters and the ^{10}Be product were also found

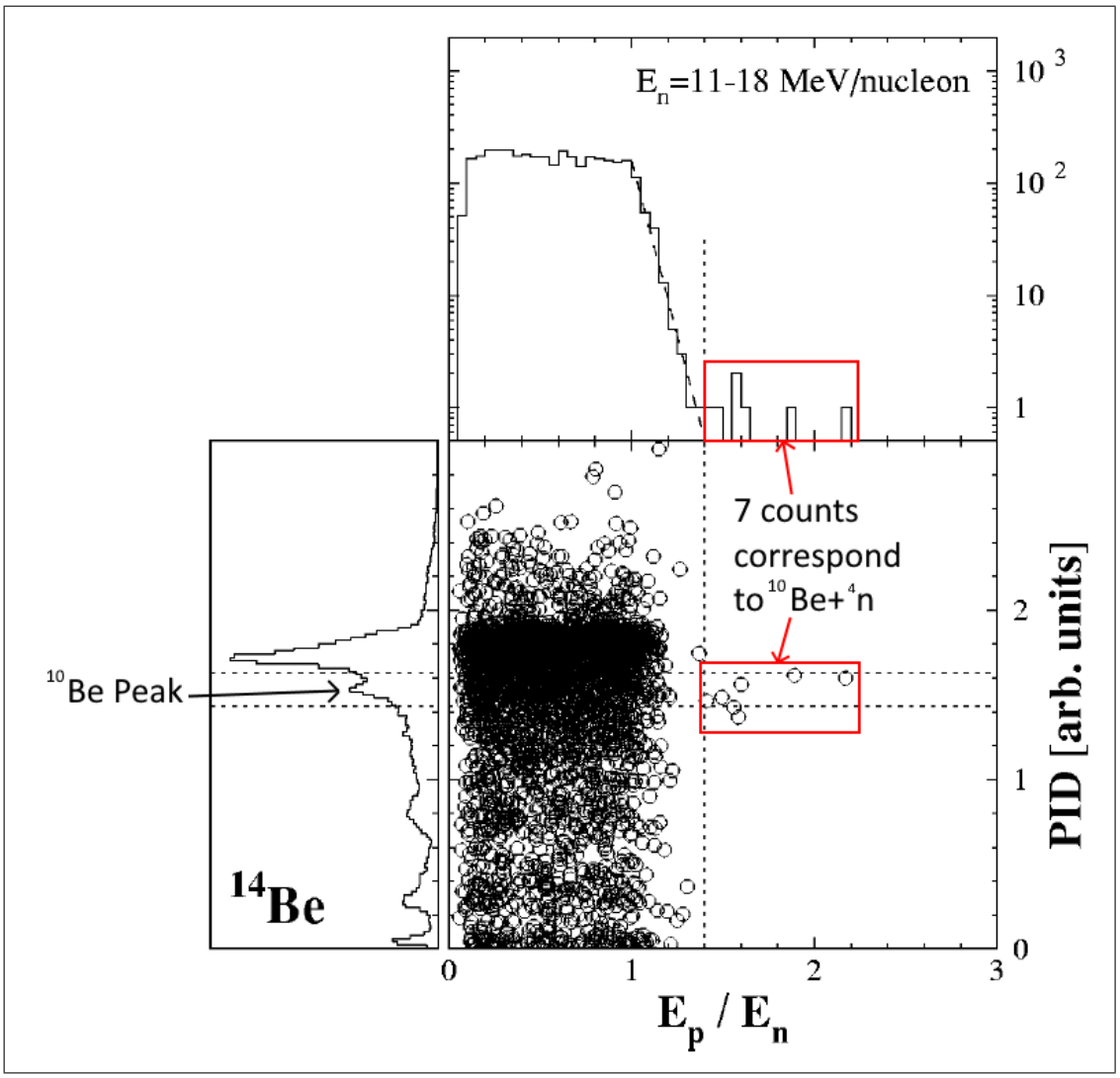

Figure 1.1: Energy from proton scattering versus energy from time-of-flight

to be consistently close to 180°, which would be most consistent with tetraneutron detections, and the energy per nucleon of the corresponding ^{10}Be were also found to be high, consistent with what would be expected from a tetraneutron reaction.

Assuming these arguments are valid, the next potential explanation could be background. Several potential sources of background were examined. The first was neutron pileup, which means that the same neutron is measured multiple times in the

same module of the DEMON detector giving an artificially high value for the proton energy detected. To attempt to rule this out, a Monte Carlo simulation was developed which generated expected results given pileup and compared the results to the background measured from the other ion breakups of ^{15}B and ^{11}Li. The expected background counts in the neutron cluster region were consistent with the measurements from the other ion beams, with 0.3 and 3.3 background counts expected in this region for the ^{15}B and ^{11}Li, which had 0 and 4 respectively. The ^{14}Be had a predicted background in this region of 0.2, yet had the seven counts in the neutron cluster region. Other sources of background were ruled out based on a few arguments. Gamma-ray sources were assumed excluded because they would be rejected due to their time-of-flight measurements being inconsistent with neutrons from the breakup. Another argument is that the correlation with the ^{10}Be does not appear consistent with background from other light charged particles, which would be expected to be independent of the channel.

To interpret what these counts must be, one should consider the time-of-flight from the reaction to the DEMON detector. The distances have a minimum of about 3.5 metres, and making the most conservative estimate for the time-of-flight, one would find a value on the order of $10^{-8}\,s$. The lifetimes of unbound resonances are typically on the order of $10^{-20}\,s$, meaning these detections could only correspond to bound particles. Given this analysis, one could conclude from this experiment that there are bound tetraneutrons. There are an abundance of theoretical predictions that the tetraneutron should absolutely not be bound, which means that this claim should

be taken with heavy skepticism, considering that it would go against much of our understanding of nuclear physics.

1.3.2 Discussion on GANIL Experiment

One crucial assumption in the analysis of the GANIL experiment is that the neutron clusters are detectable from elastic scattering with protons. More recent analysis suggests that this is not a valid assumption, due to the expected low cross-section of tetraneutron scattering with protons. (11) Tetraneutrons would necessarily have very low binding energies, as explained in an earlier section. This would make the tetraneutron very diffuse, with a large radius. As the analysis of elastic scattering from protons can be done largely ignoring the potential inside the tetraneutron, one can reasonably calculate this expected cross-section. The rate of detection in the GANIL experiment would be four orders of magnitude higher than this cross-section would give, making it very unlikely that the tetraneutron could be responsible for the reported events.

A further analysis, taking into account this issue, turned to searching for how to interpret these events as a tetraneutron resonant state. (12) The analysis had concluded that neutron pileup was not an adequate explanation for the counts, however, this assumed no correlation between the neutrons. If there were a resonant tetraneutron event, the resulting neutrons would have correlation in their trajectories, possibly leading to more counts in the DEMON detector. If this were the case, it would be consistent with a resonant tetraneutron with a resonance energy at 0-2 MeV, with

a width on the order of a few MeV. This would still be a good explanation for the behavior seen, while also lining up better with theory.

1.3.3 RIKEN Experiment

In 2016, an experiment at RIKEN in Japan was claimed to have found candidate resonant tetraneutron counts from the reaction $^4He(^8He, ^8Be)4n$. (13) The results claim four candidate counts clustered near the threshold of decay for the four neutrons. This experiment, in contrast to the GANIL experiment, finds evidence of a resonance from the missing mass spectrum, as opposed to attempting to directly measure neutron clusters. This allows the potential of measuring much shorter-lived particles, resonant tetraneutrons, as opposed to the relatively long-lived particles implied by the long time-of-flight in the GANIL experiment.

This experiment involved a high-energy (186A MeV) ^8He beam reacting with ^4He in a liquid helium target, forming ^8Be and four neutrons. The ^8He beam is formed from a ^{18}O beam bombarding a beryllium target, which created a beam with 99.3% purity. ^8Be is an unstable isotope, meaning it breaks up into two alpha particles soon after the reaction. The alpha particles go through a spectrometer which measures their momenta. This is used to obtain a missing-mass spectrum, which gives an indication of the amount of energy given to the four neutrons.

To measure the energies for the missing mass spectrum, the momenta of the two alpha particles were measured. Their momenta were measured by the SHARAQ spec-

trometer, which has a resolution of 1 MeV. The momentum of the beam also had to be measured for each event as it had a spread of 1%, making it necessary to know in order to correctly interpret the measurements for the alpha particles. The measurement of the two alpha particles is potentially advantageous for this measurement because it reduces the signal-to-noise ratio. From calibrating these factors with a hydrogen beam, the systematic error was found to be 1.25 MeV.

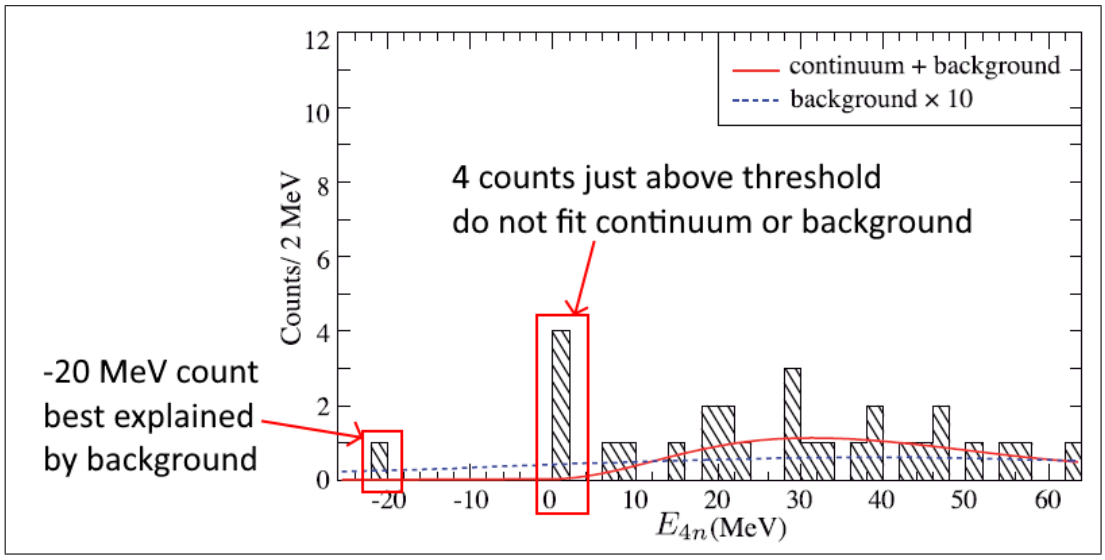

Figure 1.2: RIKEN missing mass spectrum with tetraneutron candidate states

Twenty-seven events were observed in total. The missing mass spectrum would be expected to have two components contributing to the counts, background and continuum corresponding to the four neutrons breaking up. In the spectrum, however, there are four counts very close to the threshold, in a region where the continuum should not contribute. There was also one count at around -20 MeV, another region where the continuum counts should be zero and only background can be expected. This one count can therefore be assumed to be background, as it does not appear to

have any physical significance due to restrictions from the binding energy of ^{8}He.

To determine the significance of the four near-threshold counts, a statistical analysis was carried out. A trial function was used with estimated background and continuum contributions from the theoretical calculations. This allowed the calculation of bin-by-bin goodness of fit, which gives an idea of how significantly different the bin values are from what is expected from these contributions. The deviation from the expected value for the near-threshold bin was very high, indicating that the number of counts in this bin was statistically significant. The significance was given as 4.9σ, which assuming no unknown systematic errors accounting for the statistics, would make it a statistically significant discovery. Given the properties of the peak, this would correspond to a tetraneutron with a resonance energy of 0.83 MeV, with a statistical uncertainty of 0.65 MeV and the systematic uncertainty of 1.25 MeV.

Based on the resolution of the missing-mass counts, an upper limit was placed on the FWHM of the resonance of 2.6 MeV. This is a potentially important piece of information as the theoretical estimates for the width of the tetraneutron resonance vary.

1.3.4 Discussion on RIKEN Experiment

This reaction was chosen because it was ideal for studying weakly bound systems such as the tetraneutron. This experiment involves the measurement of two charged particles, as opposed to measuring one charged particle and an uncharged particle

in the case of the GANIL experiment. The detection methods are also more reliable than in the GANIL experiment, which relied on tetraneutrons transferring energy through elastic collisions with protons, which is an assumption that is likely an invalid explanation. The GANIL experiment could potentially be accounted for by resonant tetraneutrons, while the RIKEN experiment, while not unexplainable by bound tetraneutrons, is primarily explained by a tetraneutron resonance. The use of the missing-mass spectrum reduces some of the assumptions used in the GANIL experiment, and can be used to more directly detect states with much shorter lifetimes, like the tetraneutron resonance. Despite this, the statistics are still a very low four counts. Even given the unlikeliness of the measurement, higher statistics in further experiments will be needed to increase the confidence in the validity of the discovery.

There is one lingering concern with the RIKEN experiment, which is that of the two alpha particles. The analysis assumes that the reaction $^{4}He(^{8}He, ^{8}Be)4n$ is the only contribution, and all other reactions do not contribute to the events measured. One alternative that may not be distinguished is the breakup of ^{8}He in the helium target, which would instead give the reaction $^{4}He(^{8}He, \alpha\alpha)4n$, where no ^{8}Be is formed at all. Such an ambiguity is something future experiments would need to avoid in order to give a clearer picture for evidence of the tetraneutron resonance.

1.3.5 Further Experimental Searches

There have been attempts to replicate the findings of these experiments. Subsequent to the original experiment at GANIl, an experiment at GANIL-SPIRAL

investigated the tetraneutron system through a ^{8}He beam reacting in a deuterated polypropylene target in order to react with deuterium. (14) Several different reactions were studied, one of which was $^{8}He(d,^{6}Li)4n$. This experiment, failed to find any evidence of tetraneutrons, though had a large contribution from carbon contamination in the region of the missing mass spectrum where bound tetraneutrons could be expected. If the background were reduced, this experiment could give more evidence of the tetraneutron resonance, or give evidence to rule out the hypothesis that the four-neutron halo nuclei form tetraneutron resonances.

1.4 Theoretical Searches

Given the interest in the topic of tetraneutrons, along with the experiments supposedly demonstrating their existence, there have been several theoretical studies looking at how the tetraneutron may fit into modern nuclear theory. There are a few methods that were used, some of which predicted resonances, and others predicted there could be no tetraneutron resonances. Those that did have different resonance energies and widths, which can be compared to the previous experiments and those in the future to understand the predictive powers of different theoretical approaches. Consistently, however, there are no theoretical approaches that predict bound tetraneutron states, and they are largely ruled out by theory.

1.4.1 Bound Tetraneutrons

A bound tetraneutron would involve a nuclear potential forming negative energy levels, the bound states. This requires a strong attractive force between the neutrons, which would have consequences in neutron-rich nuclei. If neutrons could be bound, why does the neutron drip line exist, and how can nuclei form at all? An attractive force strong enough to bind neutrons into the nucleus would necessitate that any extra neutrons added into a nucleus would always have an incremental binding energy, regardless of how many protons were in the nucleus; it would be able to bind to the neutrons alone. As we know this does not happen, some limit must exist on the binding of neutrons. This does not necessarily rule out any attractive force, simply one that is strong enough to bind neutrons. A claim of a bound tetraneutron would then have to explain why four neutrons can bind together in the absence of a proton, but at the same time have the neutron drip line limiting the number of bound neutrons in a nucleus.

There has been some theoretical analysis into the possible existence of bound tetraneutrons. (4) There are models, such as AV18/IL2, that can be modified to attempt to introduce a bound tetraneutron. There are a few different ways this can be done that involve different forces between nuclei; in this case, nucleon-nucleon (NN), 3-nucleon (NNN) or 4-nucleon (NNNN) forces could apply to the tetraneutron. From experiment, the NN forces are fairly well constrained, and modification in any way to form a bound tetraneutron causes many disruptions to other nuclei with well-known binding energies. NNN and NNNN potentials could potentially have the same issues,

given that many nuclei will have triplets of nuclei which will be affected. One potential solution is to introduce forces that only affect certain isospin channels. For example, in a tetraneutron, all NNN forces will be between three neutrons, which constitute isospin $\frac{3}{2}$ triples. Nuclei like ^3H and ^4He have no such triples, only T=$\frac{1}{2}$ triples, meaning they would be unaffected by a force in the T=$\frac{3}{2}$ channel. While this is adequate to form a bound tetraneutron with minimal effect on some other small nuclei, larger nuclei like ^5H and ^6He will have such triples which will cause these nuclei to be more strongly bound than seen in experiment. From this it is clear that more forces, those that act repulsively to lower the binding energies for more massive nuclei, would be required to allow these forces to exist with such a high strength.

There are more arguments to why a bound tetraneutron is unlikely. Limits can be placed on the tetraneutron binding energy due to the absence of decays into tetraneutrons. For example, ^8He is bound and does not decay into ^4He and a tetraneutron, which means that the tetraneutron must have a binding energy less than 3.1 MeV in order for this to not be a favorable decay. (8) An even more confining decay is $^5H \rightarrow {}^3H + 2n$ as this shows that the two neutrons are less bound to the nucleus than the proton, which would not be the case if the four neutrons could be bound into a tetraneutron. From this, and the failure of the modeling, it appears very clear that theory completely rules out the bound tetraneutron.

1.4.2 Tetraneutron Resonances

Resonances exist in the complex energy plane, with complex energy eigenvalues. This gives rise to the peaks - resonances - in the probability of finding a system in a certain energy state. Resonances can be found from the complex energy plane, where the real value corresponds to the resonance energy and the imaginary component corresponds to half of the width. Resonances also correspond to poles in the S-matrix, which describes the relationship between states of the system through scattering. If one were to find the S-matrix for a given system, then the resonances could also be derived from this. These are some of the methods used in the theoretical searches for the tetraneutron resonance.

Following the analysis for binding a tetraneutron through modified forces, the same can be thought of for resonant tetraneutrons. (5) This analysis, as before, starts out with a NN force that well describes the experimental observations, then introduces a T=$\frac{3}{2}$ NNN force, as before. This time, however, the force is allowed to be weaker and vary over a range of strengths. This can then be used to calculate the resulting values in the complex energy plane for the tetraneutron resonance. What is found is that, while a weak force may give a high resonance energy with a large width, the resonance energy that would be required to explain the experiment at RIKEN would need to be very strong with a strength scaling of about -30 MeV. With this model, bound states of several other nuclei would also be predicted that are known to not exist from experiment. For example, ^4H, ^4He and ^4Li all gain bound states in this model that are inconsistent with experiment. This shows that this method fails as a

method for finding the tetraneutron, even as a resonance.

Another theoretical method used to find resonances in the tetraneutron system is *ab initio* theory, particularly the no-core shell model and no-core gamow shell model. These models make some straightforward assumptions, such as each nucleon being point-like, non-relativistic and an active part of the calculation, as opposed to there being a 'core' as is typical in shell model calculations. (15) It also assumes realistic NN and NNN interactions, as well as a harmonic oscillator basis, which simplifies calculations though can lead to some incorrect behaviors. Using this method, a relationship between the scattering phase shifts and the energy can be found through convergence patterns.

Through using this method, a resonance was found in the tetraneutron system with resonance energy of 0.8 MeV and a width of 1.4 MeV. (6) This is consistent with the results from RIKEN, which gives some theoretical backing to the experimental results. This method relied on use of standard realistic NN interactions along with the methods of the NCSM and NCGSM, as opposed to the introduction of new forces required by other theoretical approaches. This different approach and its prediction of the tetraneutron resonance could indicate that this theoretical approach may be valuable. Further testing this prediction for a tetraneutron resonance could further demonstrate the merits of this theoretical approach.

1.5 Where to search for Tetraneutrons

As we have seen, tetraneutron resonances are predicted by some theoretical approaches and suggested from some experimental results. However, there are also theoretical approaches that do not agree with these experiments. Furthermore, both experiments claiming resonant tetraneutrons have potential issues. The experiment at GANIL has no direct evidence for a tetraneutron resonance besides a potential reason for excess neutron pileup. RIKEN has more concrete evidence in the form of the missing mass spectrum, however, the issue with the breakup channel allows some room for error. In both cases, the statistics are low, meaning that more experimental evidence would be valuable for demonstrating the existence of the tetraneutron resonance. Further experiments will need to find more statistics to support the theory with a method that eliminates the issues in the other experiments.

There is one common element of the GANIL and RIKEN experiments, which is the nuclei involved in the reaction. At GANIL, ^{14}Be was used, and at RIKEN, ^{8}He was used - these are both examples of four-neutron halo nuclei. This is not true for any of the reactants in the examples of reactions that did not yield evidence for the tetraneutron resonance. There are two main reasons these types of nuclei would be the most likely to yield a resonant tetraneutron if it were to exist. The first is that, due to the structure of these nuclei, pickup reactions such as $^{4}He(^{8}He, ^{8}Be)4n$ collect the core while ejecting the four neutrons in the halo. This would leave a structure such as a tetraneutron resonance intact. This is then related to the second reason, being that the neutron halo would be an ideal place for the resonance to form as

the four neutrons are confined by the field of the core. Given this, pickup reactions involving ^{14}Be or ^{8}He would be ideal under this assumption.

One such candidate reaction is $^{8}He(d,^{6}Li)4n$. This reaction fulfills many of the requirements as laid out. As ^{8}He is a four-neutron halo nucleus, with the ^{4}He core picking up deuterium and leaving the four neutrons in the halo. If the four neutrons in the halo were to form a tetraneutron resonance, it would be ejected from the nucleus during the reaction. Another reason this reaction would be a candidate for searching for the tetraneutron resonance is because, unlike with the experiment at RIKEN, there is no ambiguity with the breakup channel $^{8}He(d,d\alpha)4n$. Only the reaction of interest forms the ^{6}Li, and so if this nucleus is detected, it must have come from a pickup reaction. This reaction has already been done at the SPIRAL facility at GANIL. No evidence of a bound or resonant tetraneutron was found, however, there was a large background from carbon contamination from the target. This means that even if there were the features corresponding to a tetraneutron in the spectrum, they would be more difficult to distinguish due to the background.

The IRIS facility at TRIUMF in Vancouver, BC would be a more ideal facility for studying this reaction. IRIS uses solid hydrogen targets into which the beam is directed. As the target can be pure deuterium, this avoids issues with contamination from the target such as with the GANIL-SPIRAL experiment. In chapter 2, we will lay out the methods used to study this reaction at the IRIS facility.

Chapter 2

Method

2.1 The Study

This project aims to study the reaction $^{8}He(d,^{6}Li)4n$ at the IRIS facility at TRIUMF. Several properties of IRIS make it an ideal facility for investigating this reaction. Here, the experimental setup of the IRIS facility is presented in context of studying this reaction.

2.1.1 Experimental Setup

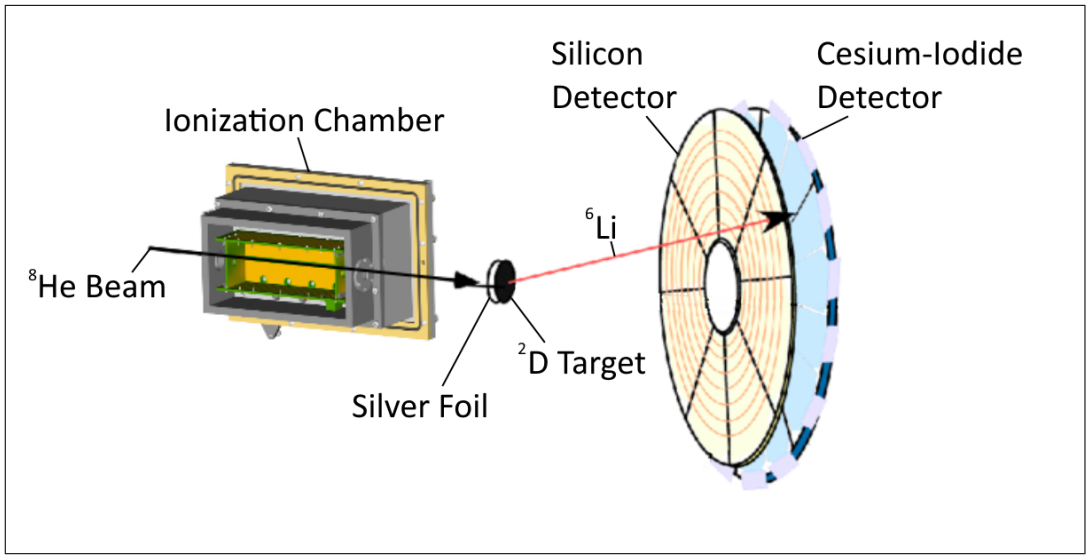

Figure 2.1: Schematic of the IRIS components involved in studying $^{8}He(d,^{6}Li)4n$.

The components of IRIS relevant to this experiment are outlined in Figure 2.1. A ^8He beam is directed to the IRIS facility, which first goes through the Ionization Chamber (IC). After this, there is a $4.26\,mg/cm^2$ silver foil on which the deuterium target is frozen. After the reaction, the ^6Li goes into the detector, first passing through a thin silicon detector, then a cesium-iodide detector thick enough to stop the ion.

The Ionization Chamber is a gas-filled detector used primarily for beam identification. Inside is isobutane gas kept at a certain pressure, for this experiment 19.5 Torr. At each end of the chamber, there is a window through which the beam passes. Being able to detect the incoming beam particle is in general important to do because it can be used to distinguish between events corresponding to the species of interest as opposed to contaminants in the beam. This may be especially important for experiments where the isotope of interest does not constitute the majority of the beam, which can be the case for some radioactive isotopes. The gas contributes to angular broadening of the beam, as well as energy loss and energy straggling.

The silver foil is a thin foil downstream from the IC. It changes between experiments, each time requiring the thickness to be measured. This process involves taking small sample areas of the foil and weighing them to get a measurement for the thickness. In this experiment, the thickness was found to be $4.26\,mg/cm^2$, or $4.06\,\mu m$. The silver foil contributes to angular straggling, energy loss and energy straggling.

One of the novel features of the IRIS setup is the use of frozen hydrogen and deuterium targets. The main chamber of IRIS is brought to a vacuum, and the silver foil is cooled to 4 Kelvin. Either hydrogen or, in this case, deuterium gas is sprayed onto the cooled silver foil, forming a target. The foil is cooled in order to freeze the gas into a solid, which allows the target to be composed entirely of deuterium. The thickness can vary, typically between $50\,\mu m$ to $100\,\mu m$. The target thickness is measured during the experiment by measuring beam transmission; a thicker target scatters more particles out of the beam. The reaction between the ^8He and the deuterium in the target forms the ^6Li product. In the target, both ^8He and ^6Li are affected by angular straggling, energy loss and energy straggling in different amounts based on their energies.

From the target, the ^6Li can hit the silicon detector. This detector is several centimetres downstream, which gives the ^6Li distance for the scattering from the reaction and other effects to spread out. It has an inner radius of $5\,cm$ and an outer radius of $13\,cm$. The distance can be varied between experiments, though in this experiment it is at $25\,cm$ from the target, corresponding to angle coverage from 11.3° to 27.5°. The primary component of the silicon detector is $100\,\mu m$ thick silicon, split into 16 rings $0.5\,cm$ and into 8 azimuthal sectors. As the ^6Li passes through this detector, it will deposit some or all of its energy into one of these sections. The detector is able to determine which of these angular bins was hit, and how much energy was deposited. The energy measured will have a broadening based on energy straggling and the resolution of the detector.

The final component is the cesium-iodide detector, behind the silicon detector. Any ^6Li that make it through the silicon will deposits its remaining energy into this detector. Any that do not are not counted, as they are unable to be identified through the two layers. As all of the remaining energy will be deposited, energy straggling will not be present in this detector, though it still has energy resolution. In combination with the silicon detector, the total energy of the ^6Li can be determined, within some resolution resulting from each detector, and an angular bin corresponding to a section of the silicon detector.

2.1.2 Missing Mass Method

The missing mass method is used to study the properties of certain nuclear reactions. It is used particularly when there is a 'missing mass' involved that is unable to be measured directly and can only be inferred from the reaction kinematics that are able to be measured. In this section, the principles behind this method will be discussed. More in-depth calculations are included in Appendix A. One useful concept in studying reaction kinematics is the concept of the Centre-Of-Momentum (COM) frame, as opposed to the laboratory frame. The COM frame is the frame in which the total momentum is zero, and also has the lowest total energy of any frame, called the invariant mass. In comparison, the laboratory frame in this experiment is the one in which the target is stationary. The 'beam energy' refers to the kinetic energy of the beam in this frame, which is 8A MeV or 64 MeV total for ^8He.

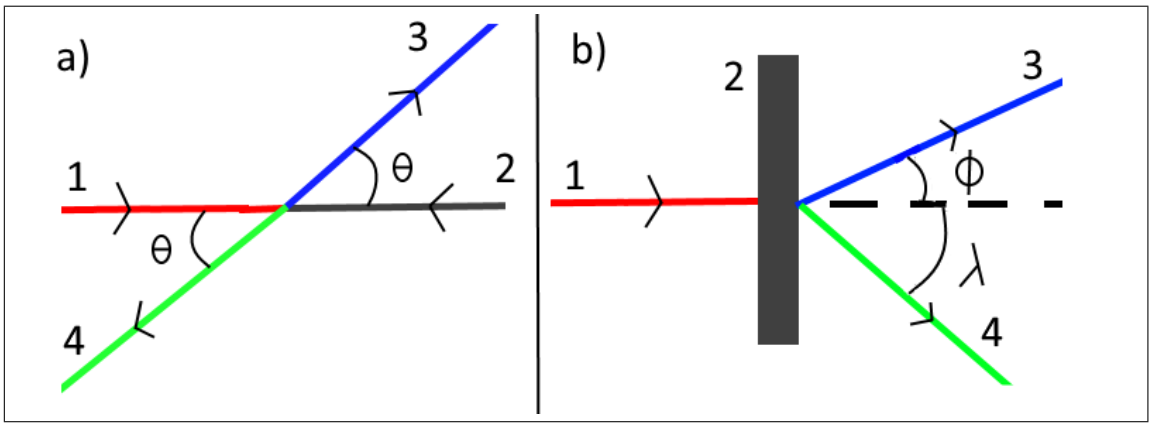

Figure 2.2: Demonstration of the COM frame (a) and the laboratory frame (b)

The type of reaction particularly of interest is the reaction with two products ('2-body'), as shown in Figure 2.2. As the momentum is zero in the COM frame, the two products must have equal and opposite momenta, with an equal magnitude p_c and equal angle θ. For given masses of these products, the corresponding COM energies and p_c are fixed by the total energy in the COM frame. This means that all reactions with these two products and available energy will have the same energies and momenta for each product, with only the angle θ varying. In Figure 2.2, 'particle 4' corresponds to the 'missing mass'. If the other three masses are assumed to be fixed, and so is the beam energy, then the COM energies will be fixed.

Varying the missing mass will mean a different partition of energy between the products, and a different value of p_c. The energy and momentum of the 'known mass', ('particle 3') will therefore be dependent on the missing mass, keeping everything else equal. As the laboratory frame is the most important in the context of experiments, the kinematics of particle 3 boosted into the laboratory frame are most interesting. In this frame, as shown in Figure 2.2, this particle will have an energy and angle

measurable by detectors in the laboratory frame. These will correspond directly with the angle and energy in the COM frame.

Keeping the 'missing mass' the same, a different θ will give different values of energy and angle in the laboratory frame that follow a locus through phase space. Points along that locus will be parameterized by θ, but all points along that locus correspond to the same missing mass. Different values of the missing mass will give a different COM energy and therefore a different locus. Any combination of energy and angle in the laboratory frame can therefore be used to find the corresponding missing mass.

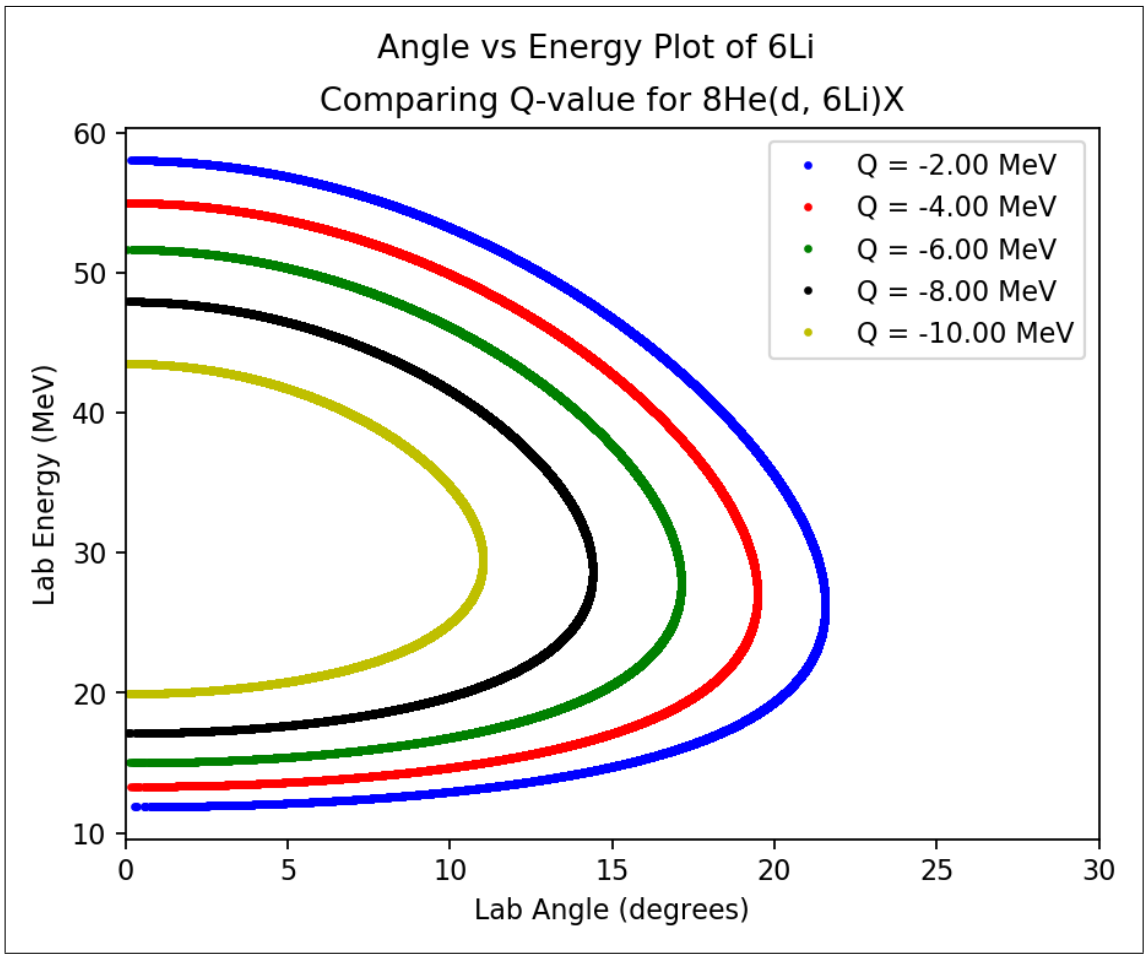

Figure 2.3: Phase space loci for different reaction Q-values

The way this is represented is using the Q-value. For any reaction, the mass is not generally conserved, with the amount of mass-energy released represented by Q. The Q-value is calculated from the equation:

$$Q = (m_i - m_f)c^2 \tag{2.1}$$

Where m_i is the sum of the initial masses and m_f is the sum of the final masses. As the initial masses m_1 and m_2, and in the 2-body case the 'known mass' is m_3, the Q-value will be dependent on the missing mass m_4 in the equation $Q = (m_1 + m_2 - m_3 - m_4)c^2$. Different values of the missing mass, and corresponding Q-value, correspond to different loci, as demonstrated for $^8He(d,^6Li)X$ in Figure 2.3, where X is the missing mass defined such as to give the varying values of Q.

One application of this method is the comparison between 2-body and higher body reactions. The missing mass in a higher body reaction could be several particles, each with some fraction of the mass. Unlike in the 2-body case, there are more free variables allowing a different partition of energy to the known mass. The energy partition in the 2-body case is an extreme case of the higher body case, where all of the unknown masses have the exact same momentum, which has a very low likelihood. All other cases give the known mass a lower COM energy, which would correspond to a higher missing mass (or an excitation energy) in the 2-body case. The different configurations will give different COM energies for 'particle 3' ranging from the energy partition for the known mass of the 2-body case as a maximum and zero energy as

a minimum. This gives a continuous distribution in the missing mass spectrum, as opposed to the delta peak in the 2-body case.

2.1.3 Studying the Reaction

Applying the principles of the missing mass method to the reaction of interest, it can be seen whether or not this is a valid method for studying the reaction. For the four-neutron breakup channel, $^{8}He+d \rightarrow {}^{6}Li+n+n+n+n$, the Q-value is $-2.15\,MeV$. This is also true for a reaction resulting in a tetraneutron with zero resonance energy, which is to say, one particle with the mass of four neutrons. Studying this reaction at IRIS, the ^{6}Li is the only product that would be detected - the four neutrons are missing from the system.

Using the ROOT (16) function TGenPhaseSpace, the phase space of the reaction can be generated showing the distributions one may expect for the measured properties of the ^{6}Li in the lab, as shown in Figure 2.4. In this figure, plots in red are the resonant reaction, while the blue are the non-resonant reaction. All angles and energies are in the laboratory frame. It can be seen that there are distinct regions for the energy and angle curves, as seen in c), and a delta peak for the Q-value of the resonant reaction, with a range of values at lower Q-values for the nonresonant reaction, as shown in d).

It becomes clear from these figures why the missing mass method is the right tool to use for studying this reaction. If the energy and angle can be measured with enough

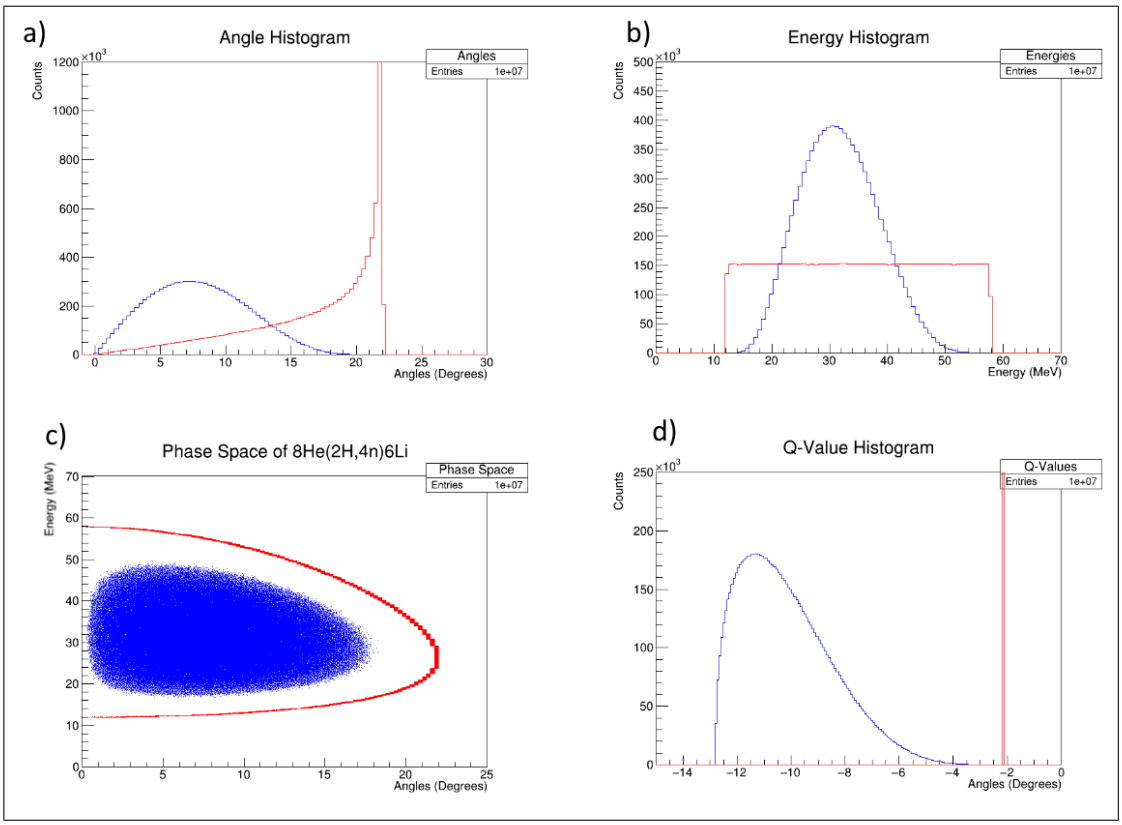

Figure 2.4: Results of phase space generation in ROOT TGenPhaseSpace

accuracy, and the Q-value spectrum can be found from those measurements, it should be possible to identify events corresponding to the resonant tetraneutron reaction as opposed to the non-resonant breakup reaction. While one can determine in principle that this method would be suited to this study, the experimental setup required to make the measurements will always introduce background and uncertainty that must be understood to be able to interpret the results.

As the Q-value is derived from the laboratory angles and energies of ^{6}Li, the effect of processes changing these values are indistinguishable from the reaction having a different Q-value. This ambiguity means that the Q-value spectrum will include broadening from different effects. Studying how the experimental setup of IRIS affects

the resolution of the measurement of the Q-value spectrum for this reaction will be the aim of this work.

2.1.4 Advantages of the IRIS Setup

One of the primary reasons this facility is able to study this reaction is due to the solid deuterium target. The primary issue in the GANIL-SPIRAL study of this reaction was the background from reactions with carbon in the target. This is not an issue in this experiment, as the only material in the target is deuterium. This is one of the advantages of the solid hydrogen targets as compared to target materials used in other experimental setups.

Identifying an event as coming from ^{8}He from the Ionization Chamber and resulting in ^{6}Li as identified in the detector can only correspond to the $^{8}He(d,^{6}Li)4n$ reaction. This is an advantage over the experiment at RIKEN, where the breakup reaction would also give two alpha particles alongside the reaction of interest. As the detector has two layers, the energy deposited into each layer allows identification of the isotope, meaning that only reactions giving ^{6}Li can contribute, and the only such reaction is the one of interest.

2.2 Simulation

A study of the reaction $^{8}He(d,^{6}Li)4n$ using the missing mass method at the IRIS facility has the potential to be an effective search for the tetraneutron. Given the

absence of background from other reactions, the primary concern for this setup would be broadening effects from the experimental setup. As noted, the distinguishability of the resonant peak in the Q-value spectrum is vital for being able to determine if events are candidate tetraneutron resonant states.

In order to do this, I have developed a simulation to generate the distributions of results as expected from the experimental setup. This simulation was built in Python using monte carlo methods. Beam events are generated in NumPy arrays, and as such all calculations are done on the entire array simultaneously. (17) This allows for faster calculations which facilitate large statistics necessary for generating continuous distributions with minimal fluctuation. With these arrays, each successive step in the process is applied as if it were a single value, using random number generation where applicable.

2.2.1 Reaction Phase Space

The most fundamental aspect of the simulation is the generation of the reaction phase space. This calculation is done in the COM frame for the simplicity of the calculation, before being boosted back into the laboratory frame. Given the masses of the reactants and available COM energy, the momenta of the products are calculated following conservation of momentum and conservation of energy. As discussed, the phase space becomes significantly more complicated to calculate as the number of products increases. The general reason for this is that there are many more free variables, and each product must have a momentum that is dependent on all the

others to maintain conservation of momentum.

For a monte carlo simulation, the ideal phase space generator would be based on a set of independent random numbers generated over fixed ranges, which is to say the same for each generation, each giving physically allowable results. Furthermore, it would be ideal to have the generated results follow the correct physical distribution, ie. even distribution in phase space. Some method for weighing the results is required to match this distribution. As has already been seen, the TGenPhaseSpace function ROOT already succeeds in doing this.

The TGenPhaseSpace function uses some simplifying assumptions to facilitate this calculation. (18) The first is to assume the reactants come together to form a single nucleus with mass equal to the invariant mass, which has mass-energy equal to the total energy in the COM frame. This nucleus is then assumed to break up into each product in successive two-body decays. This introduces the primary source of simplification, as the two-body decay is a process dependent only on the available energy, the masses of the products and a random angle. This mass will be greater than the total masses of the products, with the remaining energy difference to be divided up into the kinetic energy of the products. This is a deviation from the 'true' two-body decay, which has a fixed energy partition. This is due to the momentum conservation requirements, which are not relevant here as the final result will result in energy and momentum conservation between all the products, even if they are not maintained at every step throughout the proccess.

This method does not generate results evenly distributed in phase space. The results are generated with the cosine of the COM angle chosen from a uniform distribution, giving a uniform distribution in the laboratory energy. This is independent from spacing in phase space, though uniform distribution in both phase space and the laboratory energy are optimal. The weighting in phase space will be determined based on the products of the magnitudes of the momenta. By assigning a weighting to each of the results, an algorithm is used to filter the results in such a way as to fit better to the phase space distribution. The formula used is:

$$f_i = \frac{w_i}{w_m} - r_i \tag{2.2}$$

Where w_i is the weight for a specific result, w_m is the highest weighting calculated out of all of the results, r_i is a random number uniformly generated between 0 and 1 assigned to the specific result, and f_i is a resulting number that may be greater than or less than zero. If f_i is less than zero, the result is cut, else it remains. This formula allows a greater chance of lower weighted results to be removed and gives more highly weighted results a greater chance of remaining. This will then leave the remaining results distributed evenly in phase space.

This code was implemented in the simulation based heavily on the ROOT (16) function, though modified to meet many requirements needed in this simulation. As ROOT code runs in C or C++, there are higher speeds running loops compared to Python. This means that many of the steps in the function needed to be suited for use

with arrays as is done in the rest of the simulation. With these modifications made, the code is able to run quickly and generate phase space for many-body reactions, and is entirely relativistic, making it useful for a broad range of applications.

2.2.2 Multiple Scattering

Any material that a charged particle moves through will contribute some scattering. This will cause small deflections to the particle's trajectory for each nucleus it passes by. The primary cause of this is elastic scattering by atomic nuclei as the particle passes through a material. This effect is described by Rutherford scattering. (19) While Rutherford scattering can be applied to scattering through close passes by the nucleus, the majority of interactions will be weaker long range interactions that add up to greater cumulative scattering.

There has been study of theoretical calculations of multiple scattering. Molière theory describes in general terms how to calculate multiple scattering from a given scattering differential cross section. (20) Rutherford scattering is typically the differential cross section used in this case, however, there are some complications from this. Rutherford scattering is based on the Coulomb force, which has a strength inversely proportional to the distance. Given a relatively straight path through a thin target, the number of scatterers at a given distance goes with the square of the distance. This means that the differential cross section diverges, and so too would the multiple scattering broadening from an increasingly large number of nuclei.

The one factor not taken into account in Rutherford scattering is electrons. Rutherford scattering can only apply when the particle gets close to a nucleus, but as it passes by at a larger distance, the repulsion from electrons will screen the electric field, causing less deflection. This is how one is able to get a convergent differential cross-section and find a multiple scattering expression that can be used to describe this process. Particles may still pass close to the nucleus and be deflected at very large angles, and there are still many small deflections that add up, but they converge on a distribution of fixed width.

The form of Molière theory is somewhat complex, and not suitable for straightforward calculations such as required in this simulation. (20) Some work has been done on finding a semi-empirical form for multiple scattering using the Molière theory and measurements. The most modern such form is the Highland formula, which approximates the central 98% of the angular scattering distribution with a Gaussian distribution. (21) As there are many scattering events with particles passing closer to the nucleus and being deflected at high angles, the tails of the distribution fall off slower than for a Gaussian, meaning that only the centre of the distribution can be approximated, though this is generally valid.

Angular straggling is present in any material that an ion passes through. In IRIS, this is assumed to be the Ionization Chamber, the silver foil and the deuterium target. As the silicon detector is where the angle is measured, it is not necessary to consider the contribution to broadening. To calculate the multiple scattering for the IC and

silver foil, the physical calculator from the LISE++ program (22) is used to generate Gaussian widths for angular straggling that are hardcoded into the program. This is convenient because the beam will always be ^{8}He through these materials in this simulation, though another reaction would require new hardcoded values. In the deuterium target, there is a transition from angular straggling affecting the ^{8}He to affecting the ^{6}Li. These two isotopes will be affected differently. As a result, a built-in Highland formula function is required to take this into account.

2.2.3 Energy Loss

As well as broadening, all materials that a particle passes through will take some of its energy. In this case, the most significant cause is electronic stopping power, as opposed to nuclear stopping power. The differential of energy lost over distance is the stopping power, which is dependent upon energy. This adds some complication to the calculations for total energy lost. At higher energies or with thinner targets, the change in energy will be minimal and as a result, the stopping power can be integrated in a fairly straightforward manner. At lower energies or with relatively thicker targets, the change in energy can introduce either large errors or significantly increased computation time due to the more precise computation needed to maintain accuracy.

Similar to the case of angular straggling, energy loss is fairly consistent for the IC and silver foil. As the energy lost in both of these materials is low enough, they can be hardcoded with specific energy losses for the beam. However, as the energy

loss in the target is considered to be more significant, and the particle of interest changes from a ^{8}He to a ^{6}Li, there are more significant effects. The ^{6}Li particle has a higher stopping power in the same material compared to ^{8}He, so the energy loss calculations will have to be done twice in the target - one for the distance ^{8}He goes, one for the distance ^{6}Li goes. As the distance through the target where the reaction happens is assumed to be random, each separate beam event will have to have a corresponding distance covered by ^{8}He and ^{6}Li. Furthermore, the amount of energy the ^{6}Li has after the reaction can vary widely, which makes the possible energy loss for ^{6}Li much broader than for ^{8}He. This means that there must be some built-in energy loss function to account for different beam energies entering the target and different distances covered by ^{8}He and ^{6}Li.

While LISE++ (22) has energy loss in the physical calculator, it is also possible to generate stopping power tables for a given interaction. This allows calculations with varying energy and thickness, though with extra computation required. An interpolator is made and an integration function is used to calculate all the energy losses. As the energies are in an array, integration must be done on the entire array at once to allow reasonable computation time given the high number of counts.

The integration limits, determined by the distance through the target traversed, are not able to be unique for each event and therefore may not be considered on an event-by-event basis. To overcome this, the integration must be done with different distance 'bins', with 1 μm bins used in the simulation. First, all events are considered

and integrated together. At each step, events with an associated distance equal to that bin (for instance, after the 50th bin for a $50\,\mu m$ distance) are taken out of the integration. This way, each event can be integrated over a distance approximately equal to the distance they cover, sacrificing some accuracy to maintain some computational efficiency.

For the deuterium target, this process works because the energy will never be near the threshold energy for total energy loss. As only a small amount of energy is lost to the IC and silver foil, the energy lost to the target never approaches the threshold. The integration method works on its own in this case, even with maximal energy loss from a reaction at the start of the target. After the target, the ^6Li goes towards the detector, in which it must pass through $100\,\mu m$ of silicon. This thickness of silicon combined with the lower energy for some of the ^6Li particles gives a significant fraction of events where the particle does not have enough energy to make it through the entire layer. As the energy gets closer to zero, the stopping power changes much more dramatically. The integration method used is gaussian quadrature using an in-built SciPy function. (23) This method requires picking a number of points to do the integration in order to meet a certain accuracy. In this function, when integrating an array, the points are the same even though the integrals themselves are different. When approaching the threshold energy, which is the minimum energy required to traverse the material, the stopping power begins to vary significantly and is invalid once the particle reaches zero energy. This means that the integration becomes too unwieldy to be useful.

The solution to this is to find the threshold energy and remove all events from the array that have less than that energy. To do this, a root-finding function is employed to find the threshold energy. First, it takes the highest and lowest values in the array and carries out the energy loss integration. If the highest and lowest are both able to be integrated, ie. above the threshold, then the entire array can be integrated. If it were that neither could be integrated, the entire array would not need to be integrated as none of them would make it through the material. If, however, the upper bound is above the threshold but the lower bound is not, the root-finding algorithm is employed. At each stage, the mid-point between the last two points is tested and selecting the next points in order to close in on the threshold energy, stopping when the desired accuracy is reached. The values in the array below this value are removed, as these events are not counted, and the rest are integrated to find their energy loss.

The cutoff energy may be different depending on the distance through the target. To take this into account, the process for finding a cutoff energy is done for each distance bin. The cutoff energy at the high end of the bin is found, and all events in that bin with a lower energy than the cutoff are removed. This maintains some accuracy in the cutoff, as setting a high limit may cut out a significant fraction of events that would have made it through. This is particularly true in the silicon detector, where the highest distances of about $108\,\mu m$ are set by higher angles, but particles with energy less than the cutoff energy at this angle may not be cut off at a lower angle, only going through about $100\,\mu m$.

2.2.4 Energy Straggling

There will be some variation in the exact amount of energy lost for each particle, called energy straggling. This is simply assumed to be a Gaussian around the mean energy loss. Near the threshold energy, going below the threshold just sends the value to zero. As before, the IC and silver foil can get values from the LISE++ physical calculator (22) as they are assumed to vary very little between beam events.

Energy straggling is similar to angular straggling, coming from the interactions with many different constituents in the material, however, in this case, electrons are considered the primary source as opposed to the nuclei. The most basic approximation to this is the Bohr formula for energy straggling, (24) given by:

$$\sigma^2 = 4\pi Z_1^2 Z_2 k^2 e^4 n x \tag{2.3}$$

Where Z_1 and Z_2 are the ion and material atomic numbers respectively, n is the number density of the material, and x is the thickness. The equation gives the standard deviation of the Gaussian, σ. Comparing this formula to the values given by the LISE++ calculator shows that it is most accurate at moderate energies for the materials in use, from a bit higher than the threshold energy up to the GeV range. However, as many of our events will be near the threshold, this formula is inadequate.

As with energy loss, finding a table to interpolate from, such as from LISE++, would be ideal. However, no such table can be generated directly in the region of interest with a high enough resolution to generate accurate results. The physical

calculator is an indirect way this can be done. As seen in equation 2.3, there will be a proportionality of the straggling standard deviation with the square root of the distance. This relationship is maintained with the physical calculator, so if one were to find energy straggling for one energy and one thickness, it could be found for a different thickness. The only relationship not easily determined is energy, so if the relationship between energy straggling and energy at one thickness were found, such as for $100\,\mu m$, it could be used for any thickness and any energy covered by the relationship.

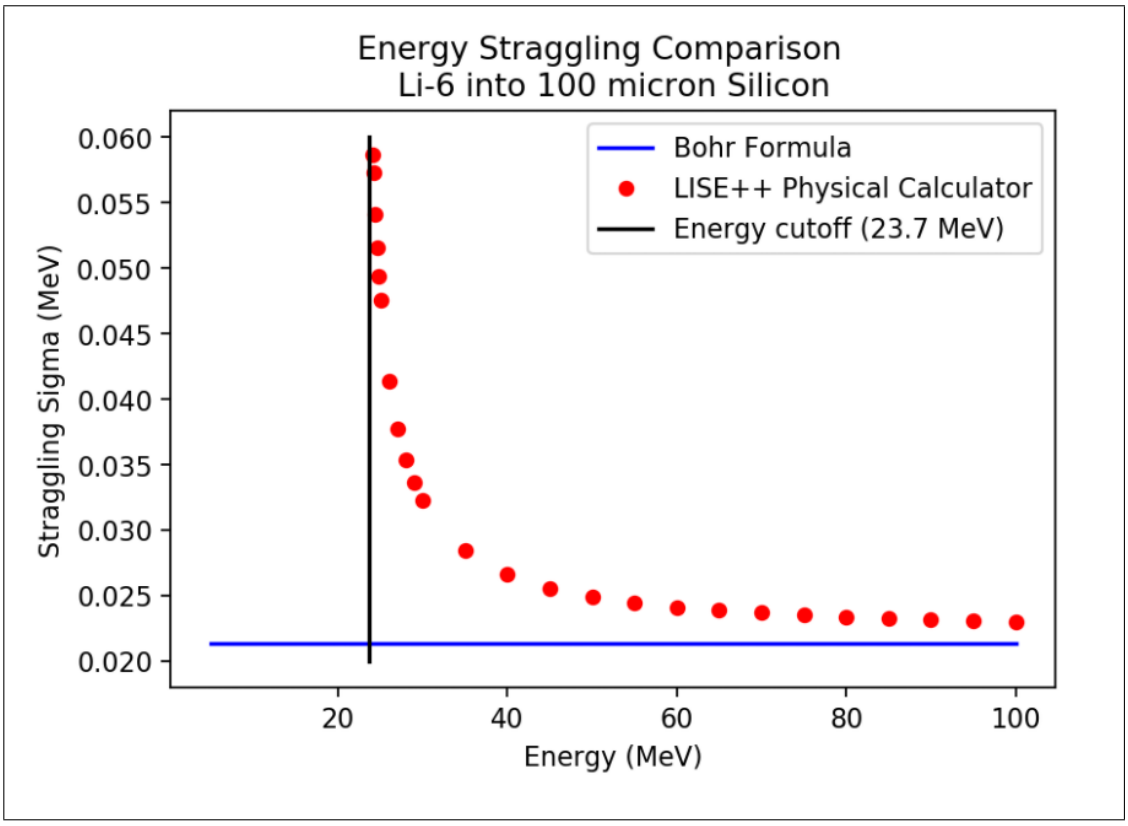

Figure 2.5: LISE++ physical calculator values compared to Bohr formula

By determining energy straggling at different points in the region of interest down to the threshold energy from the LISE++ calculator, these can be put in a file for the

simulation to interpolate from. A demonstration of this is shown in Figure 2.5. In this figure, the red points are samples of values for energy straggling from LISE++ compared to the Bohr formula for different values of energy for ^{6}Li going through $100\,\mu m$ of silicon. This needs to be done manually for all interactions in the simulation, those being ^{8}He through ^{2}H, ^{6}Li through ^{2}H and ^{6}Li through ^{28}Si. By combining the interpolation over different energies with the variation of thickness through the deuterium, the simulation can get a reasonably accurate value for energy straggling for each energy loss event.

2.2.5 Detector Resolution

The detector measures two aspects of incident particles - the energy deposited and the angular segment it hits. The energy measured comes from the energy deposited into the material through energy loss, which will be affected by energy straggling. The exact physical energy is assumed to be given by these two effects for each event, then measured by the detector with some resolution. Resolution is determined for each of the silicon and cesium-iodide detectors by:

$$\sigma_E = R\sqrt{E_{Det} \times E_{Ref}} \tag{2.4}$$

Where R is the resolution scalar, E_{Det} is the true physical energy deposited and E_{Ref} is the reference energy. The resolution is assumed to be Gaussian, with σ_E as the standard deviation. The reference energy is some energy at which the detector's resolution was measured to be R using an alpha source. The true resolution at a

given energy scales with the square root of the energy, as equation 2.4 suggests.

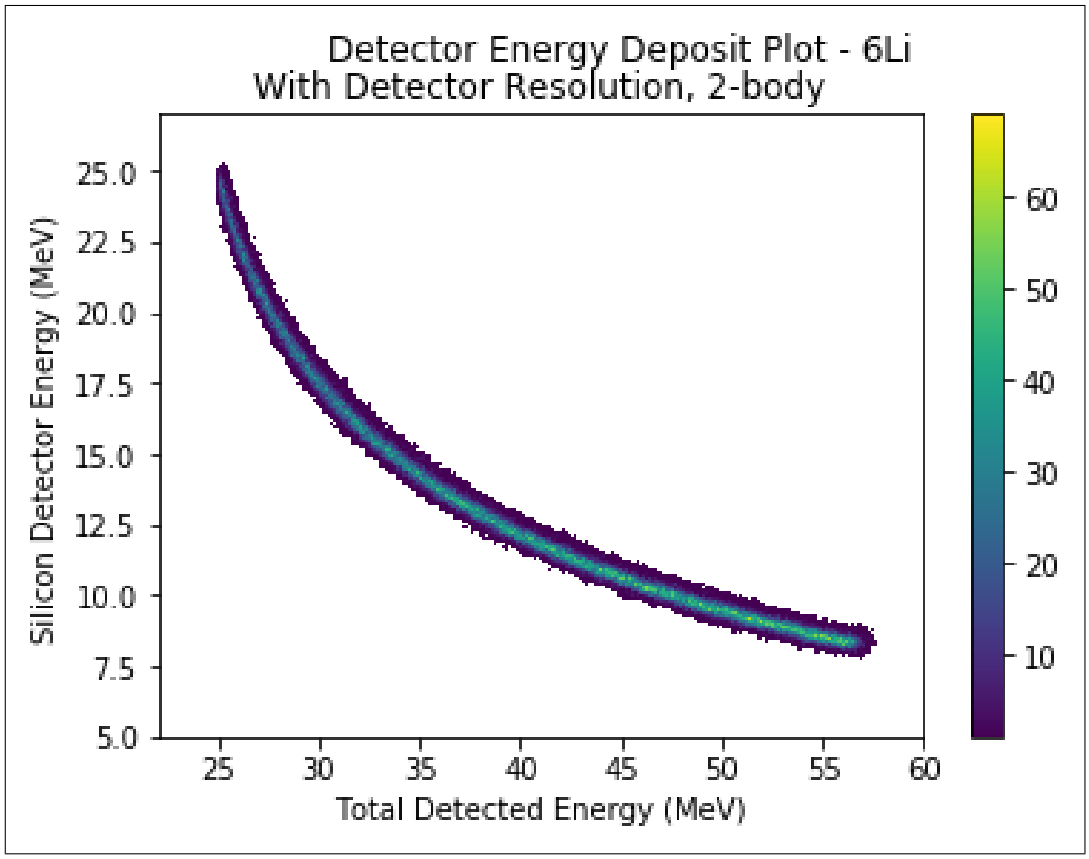

Figure 2.6: Detector energy deposit signature of $6Li$

To calculate the measured energy of all beam events, the energy loss and energy straggling are found for the silicon. The cesium-iodide is then assumed to take the remaining energy, meaning that no energy loss or energy straggling calculations need to be done for this material. Each event is then given a resolution based on its energy, and this resolution is then used to generate a value from a Gaussian distribution with the width for that beam event. The silicon detector has a resolution with a sigma of 0.25% and a reference energy of $5\,MeV$. The cesium-iodide detector has a resolution with a sigma of 3% and reference energy of $1.5\,MeV$. The two measured values from

the different detectors can be combined to get a total measured energy. One can also generate a curve comparing the energy detected in the silicon detector compared to the total measured energy. A curve like this allows distinguishability between different species, and so should allow one to determine if an event is a ^6Li event compared to another isotope like ^7Li based on the curve. An example of this curve is shown in Figure 2.6.

2.2.6 Detector Angles

The detector covers only a subset of angles due to the detector geometry, and gives information on the angles only to within certain segments. The angles covered by the detector are determined based on the radii of the inner and outer rings of the detector and the distance from the target to the detector. This distance may vary slightly based on where the reaction happens in the target. If the reaction happens at the start of the target, it has more distance to broaden giving it a higher angle, while a reaction at the far end of the target will not broaden as much and as a result go at a slightly smaller angle. Events where the ^6Li angle is too high or too low to hit the detector will not be counted. The rings on the detector are spaced $0.5\,cm$ apart, a total of 16 rings, with detection of angle only possible to within one of those bins - the exact location in the bin is not measured.

Determining the angle that a ^6Li particle hits the detector and determining in which bin it is measured will give discrete values, which means a continuous distribution would not be possible. However, a continuous distribution can be generated in the

same way it could be for real data by randomizing within an angular bin. This smooths out peaks associated with a single angular value one would see with using the mean value of the bin. The detector geometry will cut off a large section of the Q-value spectrum for the non-resonant reaction, as some of the lower values for Q correspond to small angles, less than the inner angle cutoff. The broadening can be somewhat significant from this effect, as an ion with a lower angle in a bin corresponding to a certain energy could be randomly given an energy on the higher end of the bin. This causes broadening that comes in steps, corresponding to each angular bin.

2.2.7 Beam Properties

Some of the last effects come from the initial conditions of the beam. The beam is assumed to have some lateral broadening, meaning it is centered around some point and spread out by a Gaussian. This is assumed to have a full-width-half-maximum of $2\,mm$. This is a potentially significant effect, as it will vary the angle from the centre of the detector. For comparison, the detector angular bins are $5\,mm$ across, which indicates that this effect could shift a significant portion of events into different angular bins. This is implemented with the angular straggling from the IC and silver foil, as these effects change which point in the plane of the target the reaction happens alongside the change in the angle. As angle on the detector is based around the centre point of the target, the lateral broadening will have an effect on the angle as it will take the reaction further off-axis.

The energy of the beam is also assumed to have some spread to it, about 0.15%. This is a much less significant effect compared to the broadening from effects like energy straggling, but still relevant to generating an accurate simulation. When the beam events are first generated, they are generated in an array with an assumed energy, 8A MeV, broadened by a Gaussian with the given resolution.

2.2.8 Putting It Together

All of these effects are taken into account in the simulation such that each effect adds to the next in the order they should to represent the true physical process. The initial beam energies are set based on the energy width, then the energy loss from the IC and silver foil are applied along with the corresponding energy straggling. After this, there is the energy loss and straggling for the ^{8}He through the deuterium. At this point, the reaction phase space is calculated taking into account the energies. The position in the target where the reaction happens is determined taking into account the lateral and angular spread from the beam width and multiple scattering in the IC, silver foil and target. These are used to modify the angles at which the ^{6}Li particles leave the reaction. The angular straggling, energy loss and energy straggling for the ^{6}Li are taken into account at this point. Finally, the angles and energies deposited in the detector layers are calculated.

With the angles and energies in the detector, the Q-value can be calculated. Every part of the simulation will have some effect on the calculated Q-value, either broadening it or shifting the spectrum. The primary difference between the resonant and

non-resonant reaction is the phase space, with every other effect remaining the same. Assuming that the simulation is an accurate representation of the real IRIS setup, these distributions should mimic the Q-value spectrum from the experiment.

Chapter 3

Results

In this chapter, the results of a systematic study of the simulation will be presented. Each effect in the simulation is isolated and studied for the resonant reaction with a resonance energy and width of zero. The full simulation result is then presented for both the resonant and non-resonant reactions.

3.1 Beam

3.1.1 Energy Spread

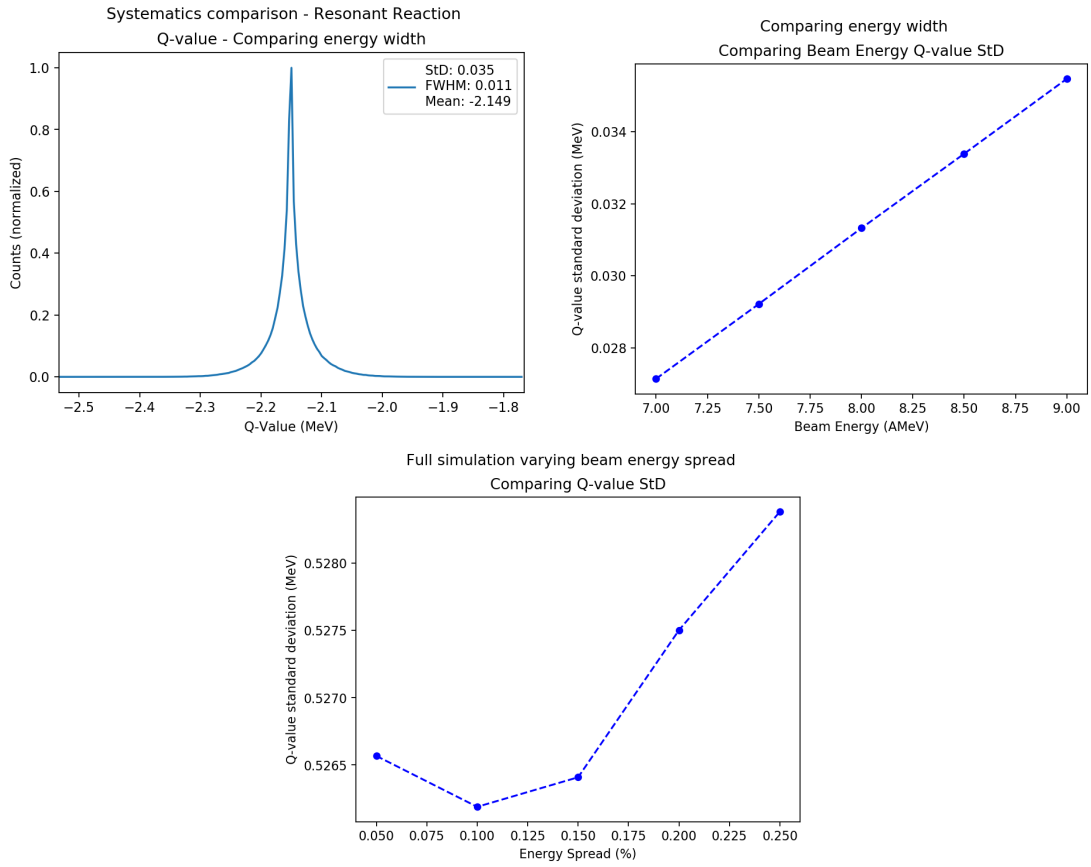

Figure 3.1: Comparing beam energy spread

3.1.2 Beam Width

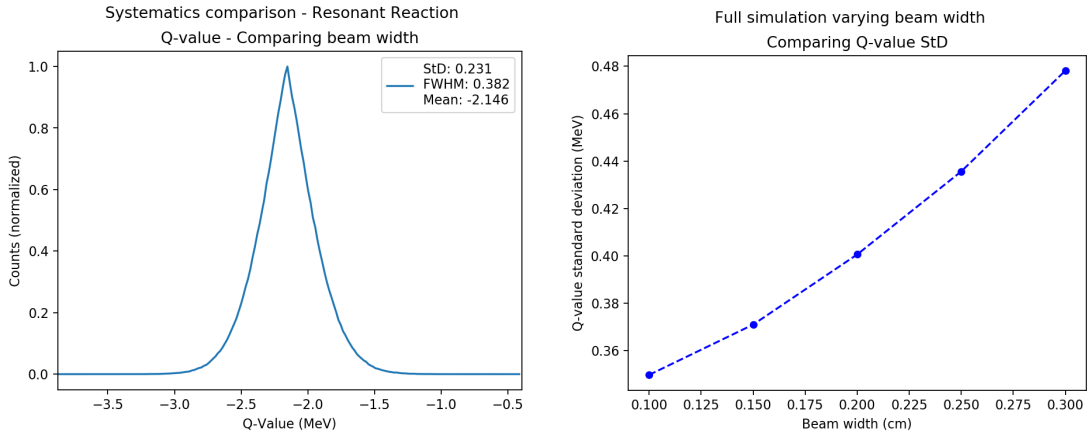

Figure 3.2: Comparing beam width

3.2 Ionization Chamber

3.2.1 Energy Loss

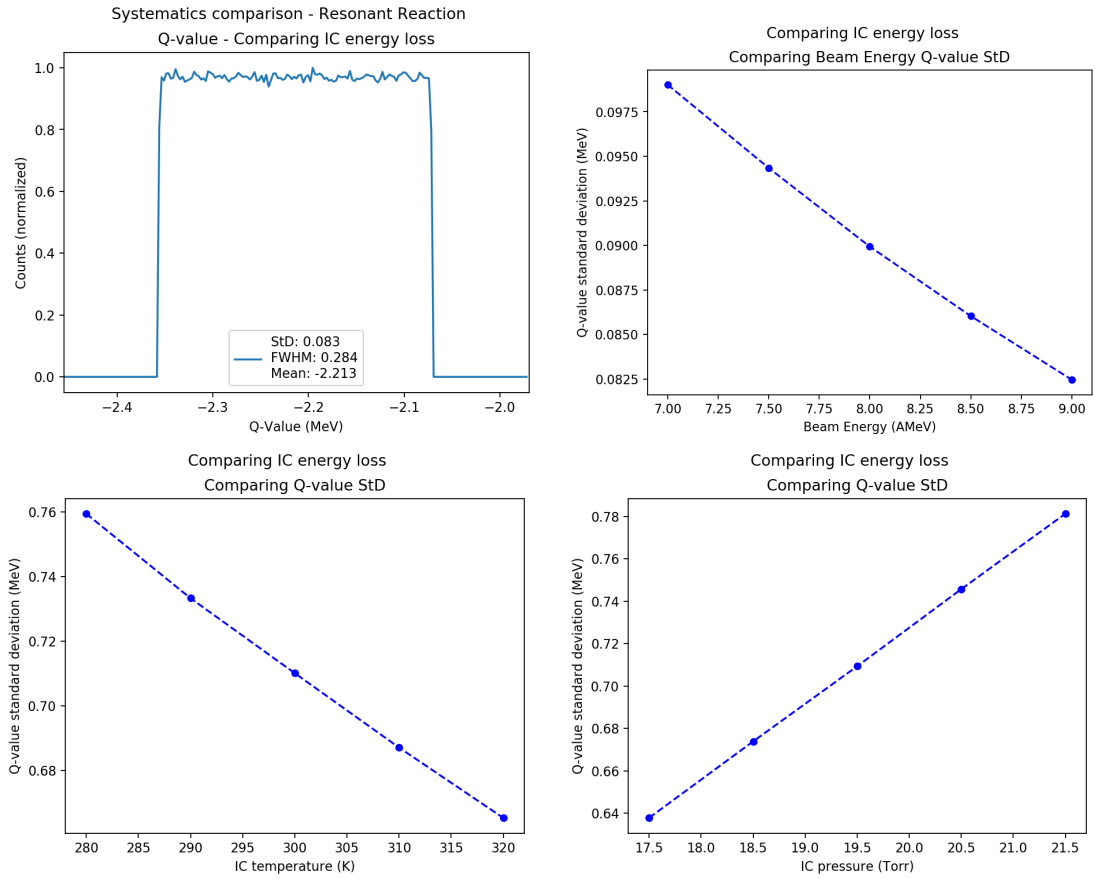

Figure 3.3: Comparing energy loss from the IC

3.2.2 Energy Straggling

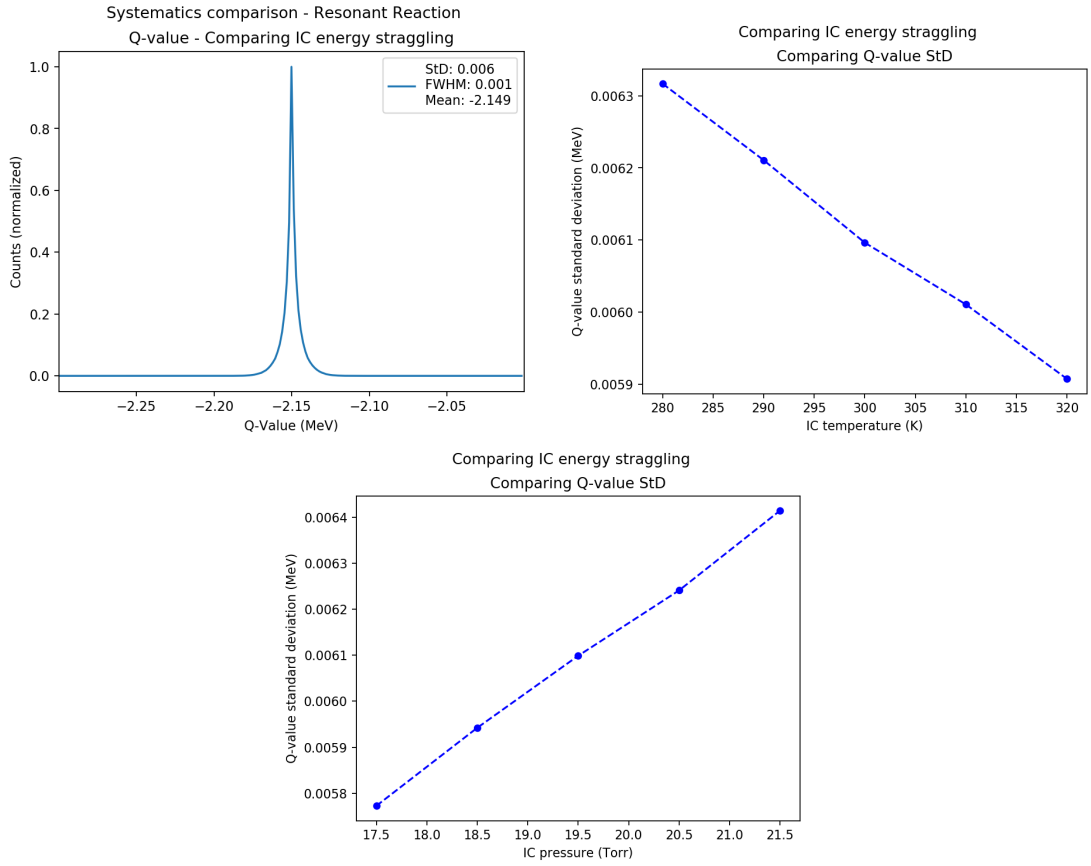

Figure 3.4: Comparing energy straggling from the IC

3.2.3 Angular Straggling

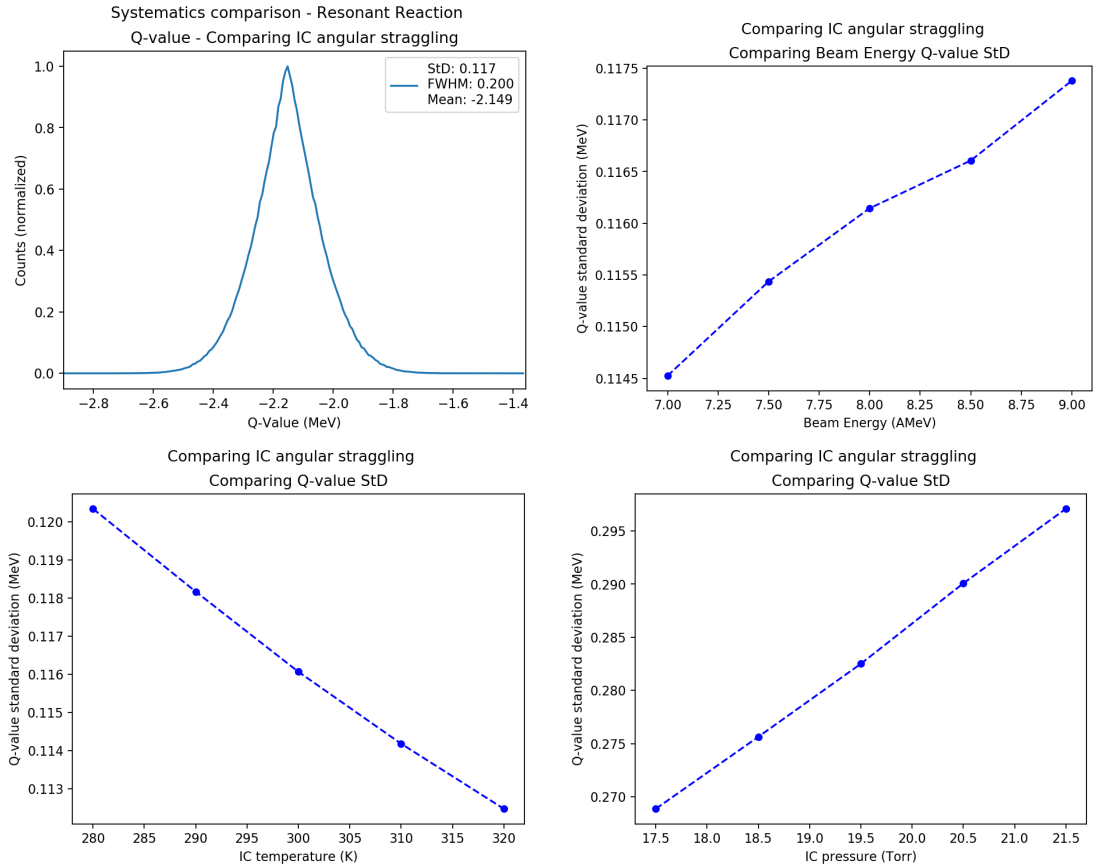

Figure 3.5: Comparing angular straggling from the IC

3.3 Silver Foil

3.3.1 Energy Loss

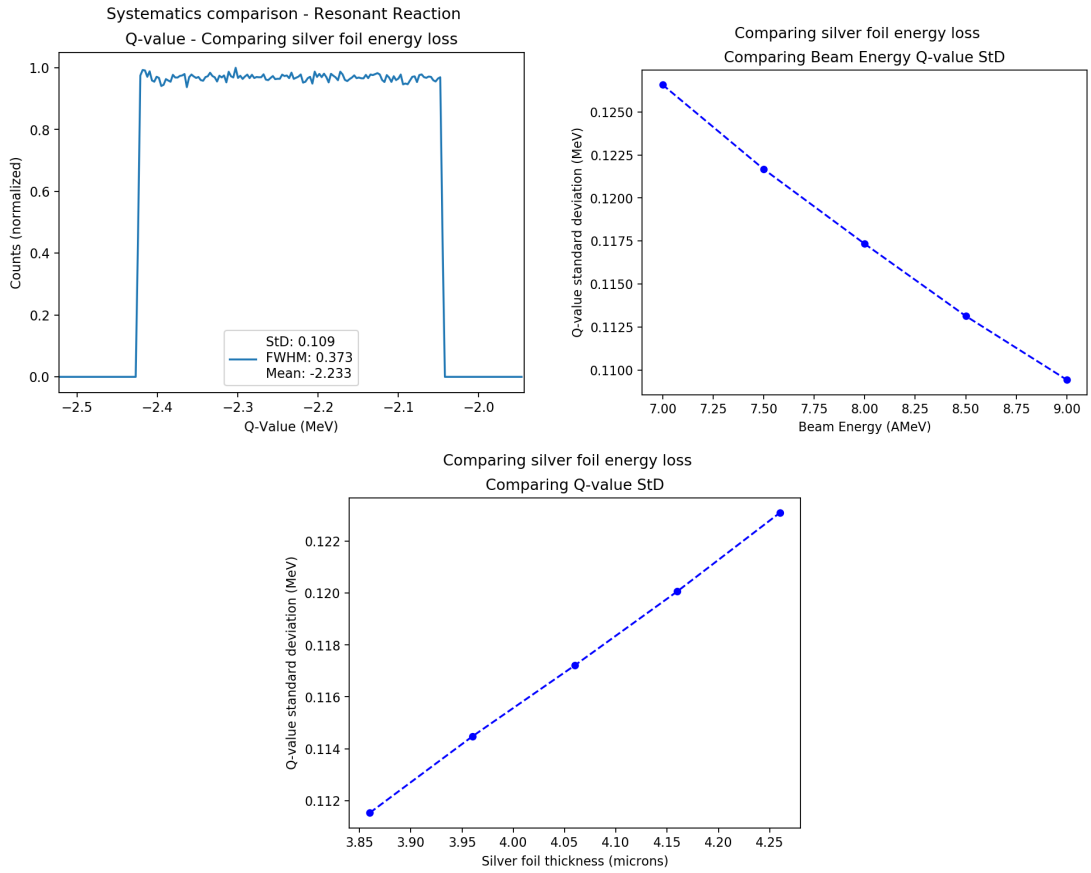

Figure 3.6: Comparing energy loss from the silver foil

3.3.2 Energy Straggling

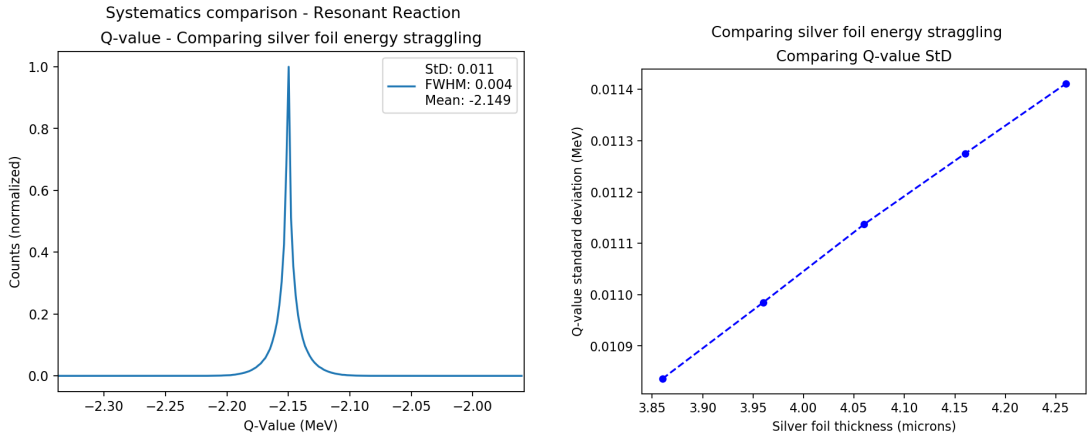

Figure 3.7: Comparing energy straggling from the silver foil

3.3.3 Angular Straggling

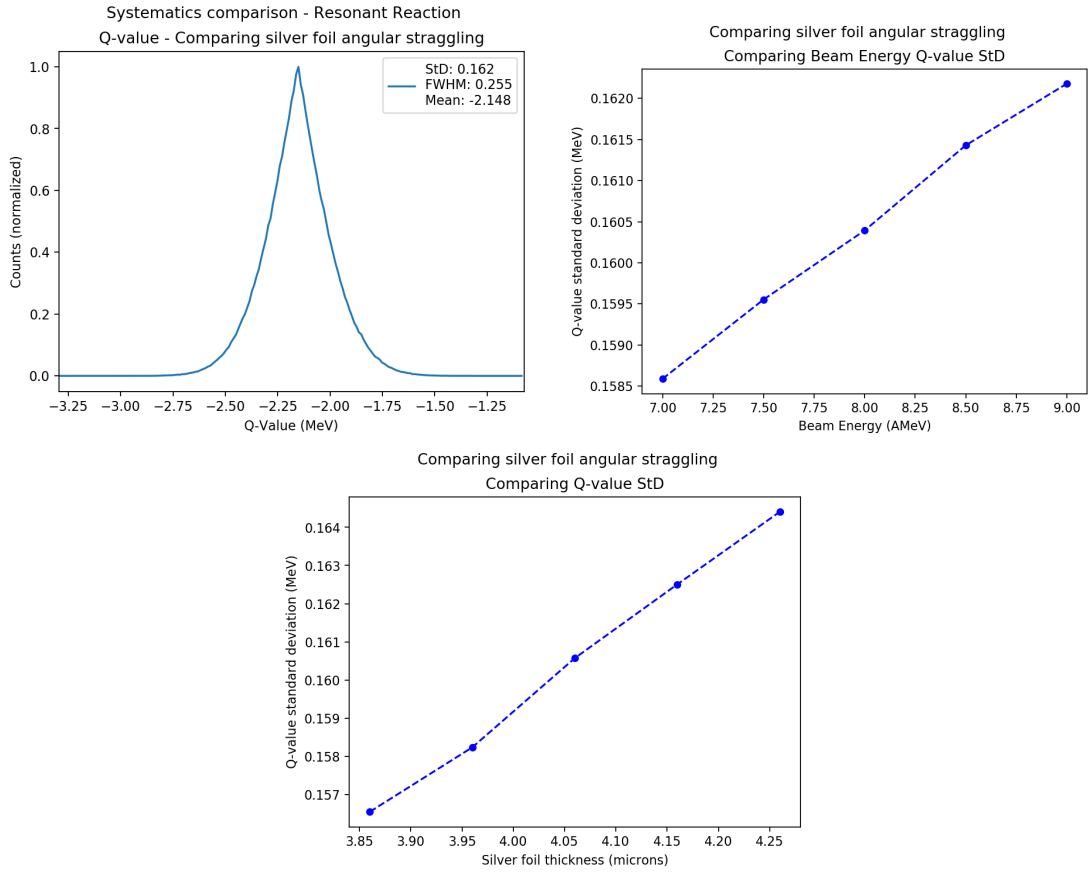

Figure 3.8: Comparing angular straggling from the silver foil

3.4 Deuterium Target

3.4.1 ^{8}He Energy Loss

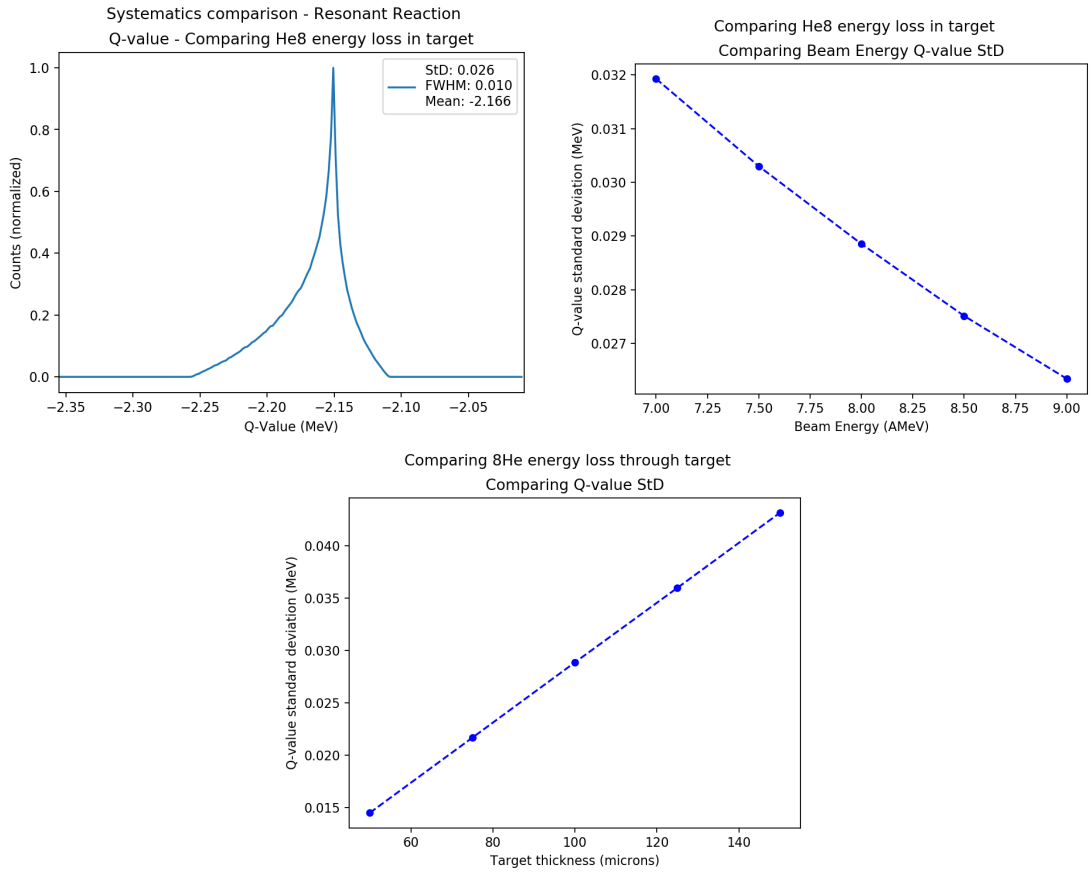

Figure 3.9: Comparing ^{8}He energy loss from the target

3.4.2 ^{8}He Energy Straggling

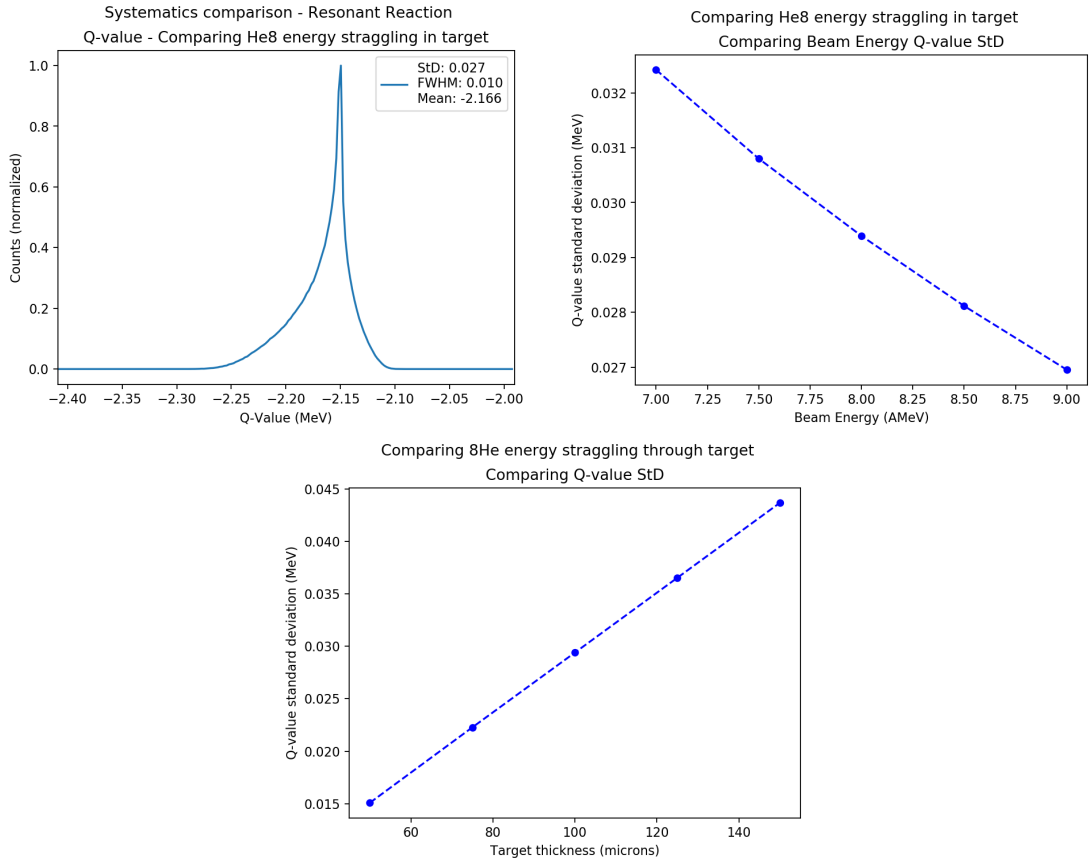

Figure 3.10: Comparing ^{8}He energy straggling from the target

3.4.3 ^{8}He Angular Straggling

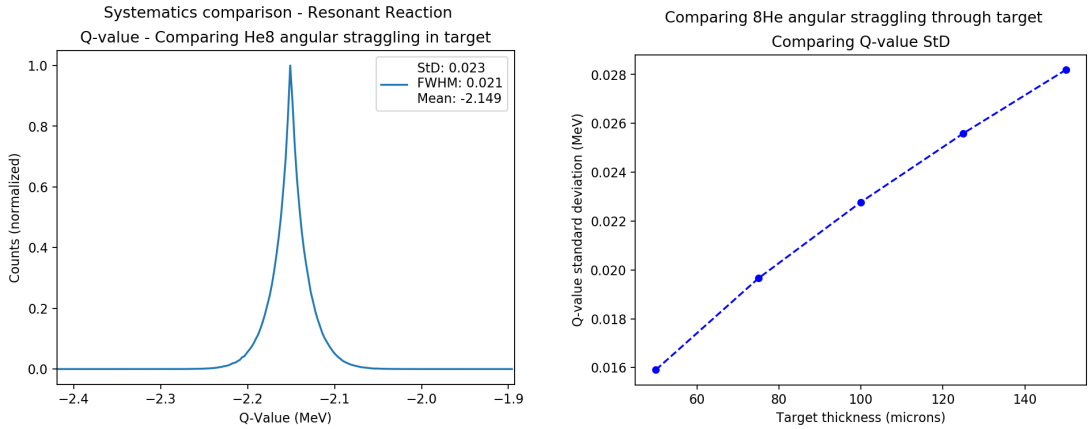

Figure 3.11: Comparing ^{8}He angular straggling from the target

3.4.4 ^6Li Energy Loss

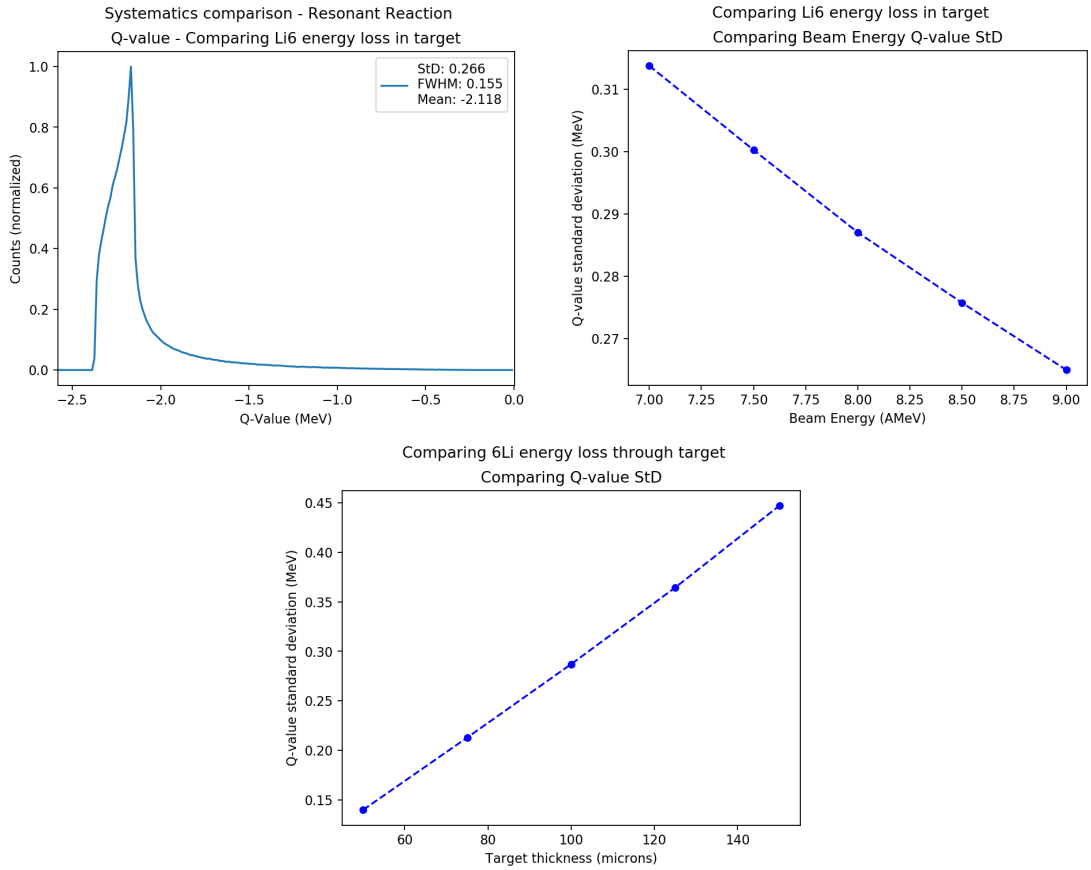

Figure 3.12: Comparing ^6Li energy loss from the target

3.4.5 ^6Li Energy Straggling

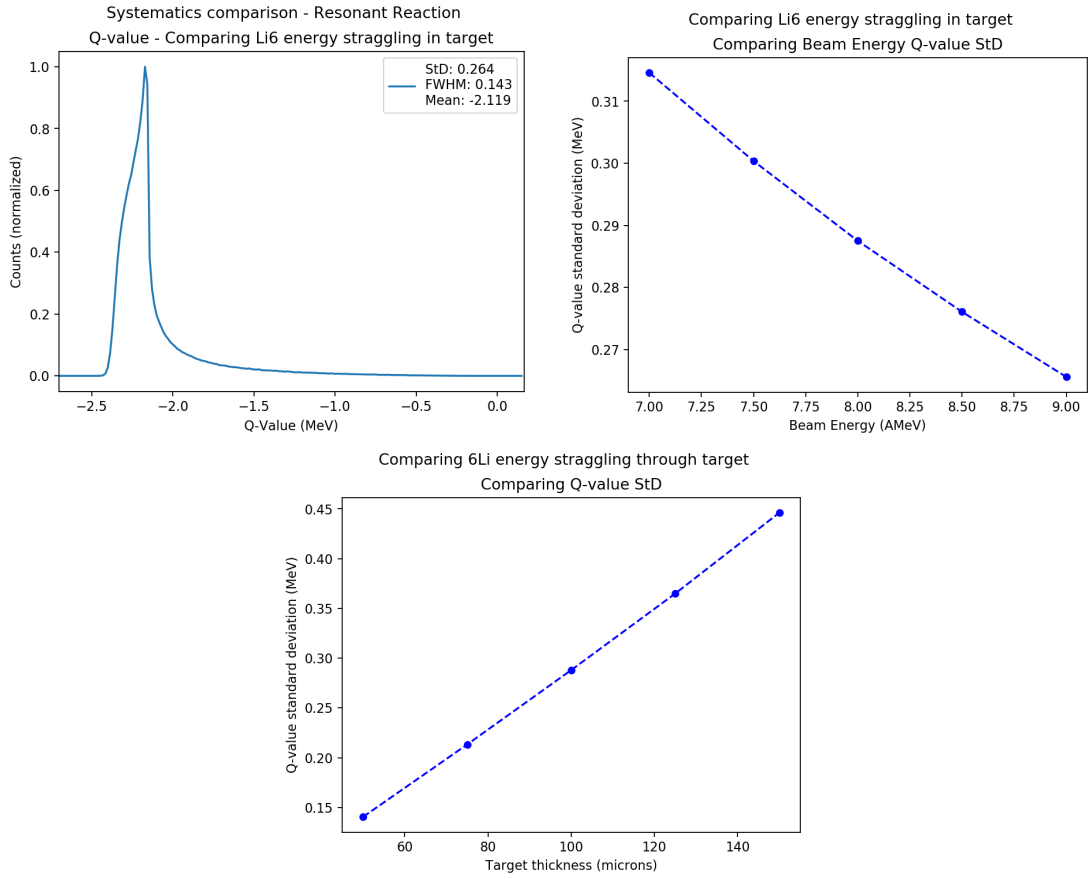

Figure 3.13: Comparing ^6Li energy straggling from the target

3.4.6 ^6Li Angular Straggling

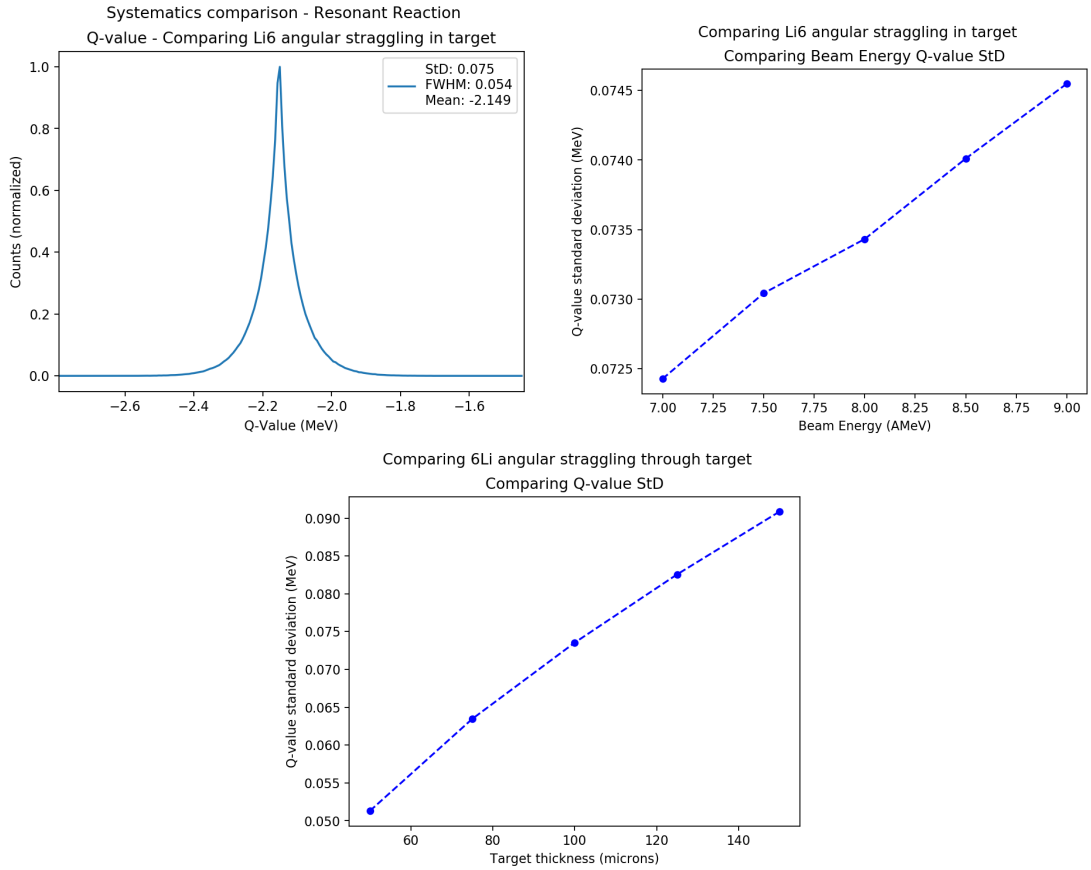

Figure 3.14: Comparing ^6Li angular straggling from the target

3.4.7 Angle Broadening

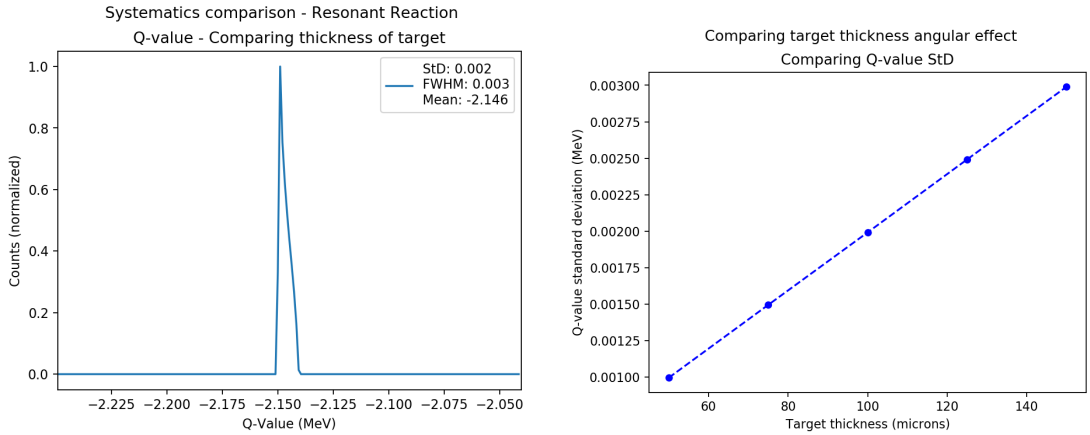

Figure 3.15: Comparing angle broadening from target thickness

3.5 Detectors

3.5.1 Silicon Detector

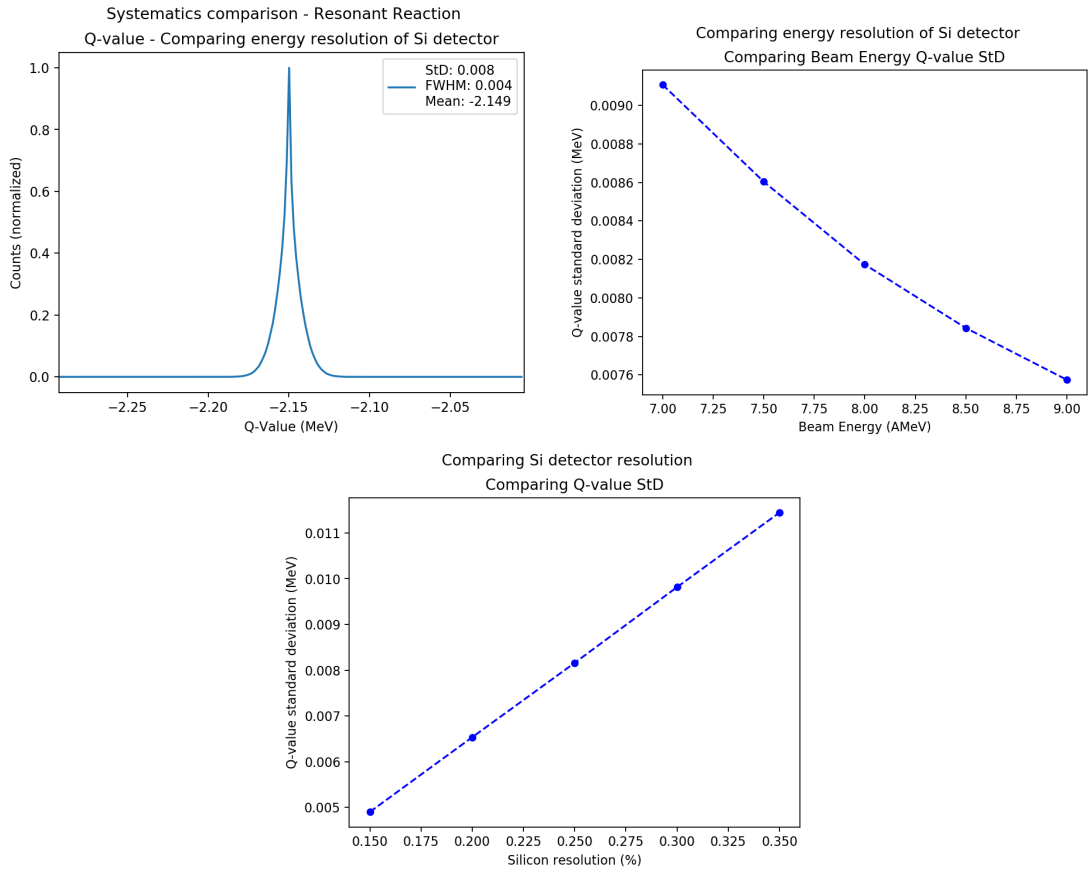

Figure 3.16: Comparing silicon detector resolution

3.5.2 Cesium Iodide Detector

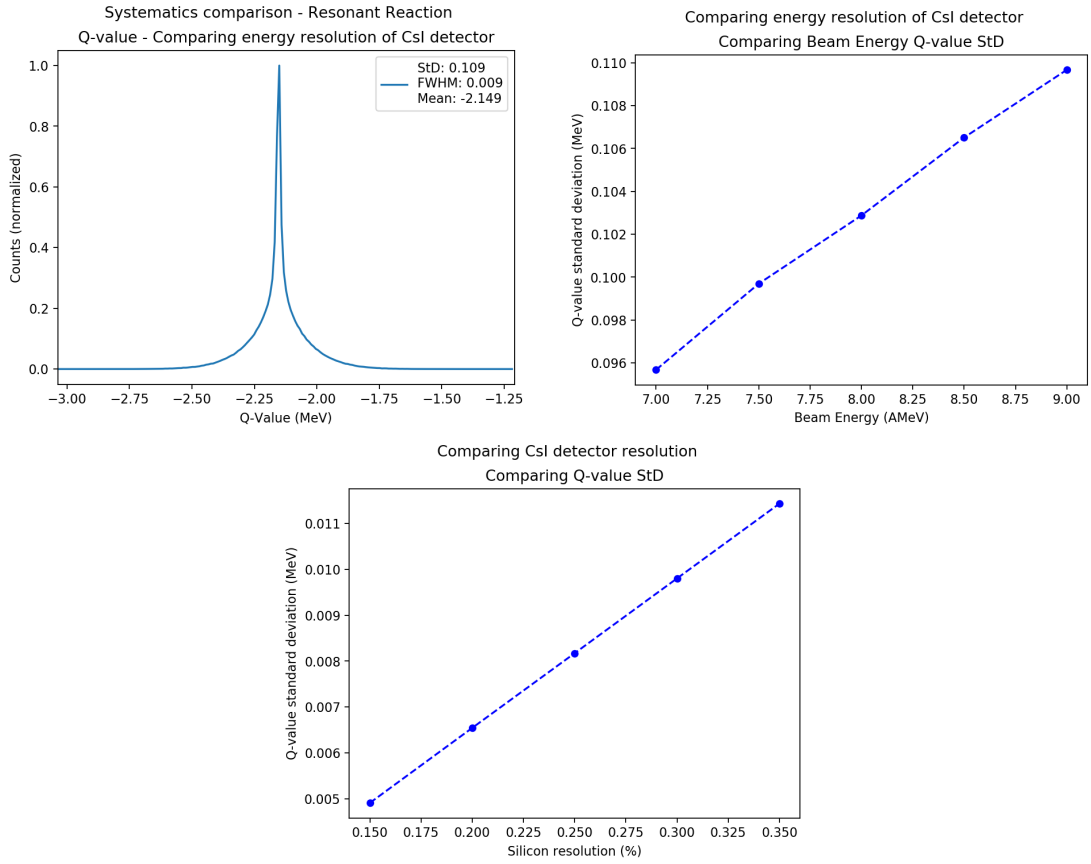

Figure 3.17: Comparing cesium iodide detector resolution

3.5.3 Angular Segmentation and Geometry

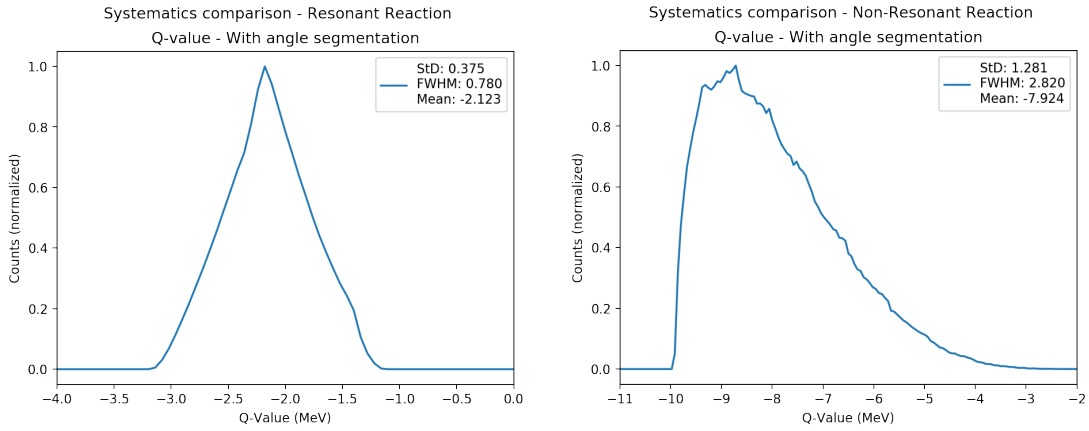

Figure 3.18: Comparing effect of angular segmentation

3.6 Final Results

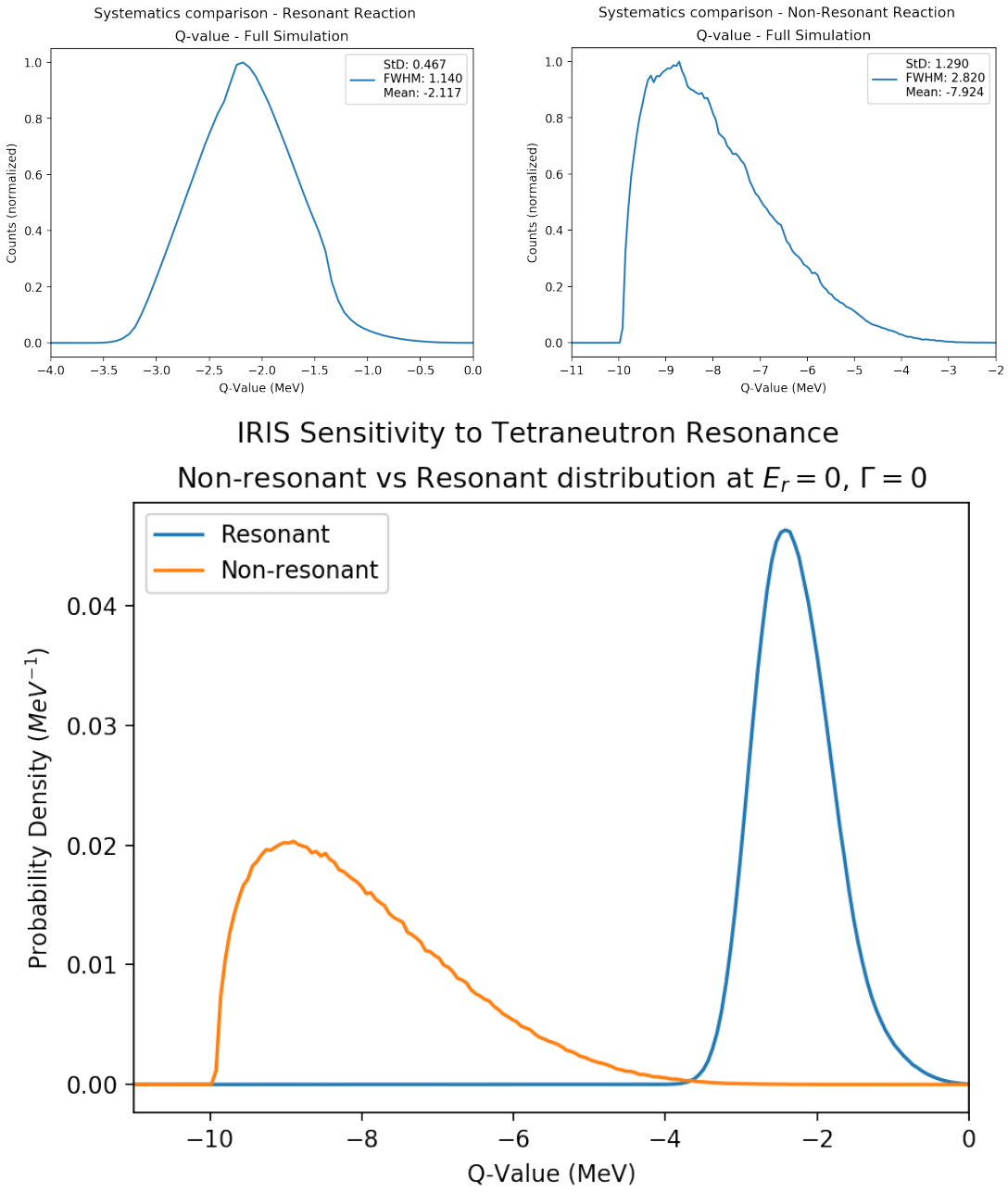

Figure 3.19: Final results of simulation for resonant and non-resonant reaction

Chapter 4

Discussion

In chapter 3, the results of a systematic study of the simulation were presented. In this chapter, the results will be examined to determine if the effects in the simulation reflect the real physics in the experimental setup. The limits from the random number generation as well as the expected results from variations in energy and angles will be discussed.

4.1 Computational Uncertainty

When generating distributions with the simulation, as random numbers are used, there will be some random variation in the exact number of counts at different values. In the histograms generated to demonstrate results, the number of counts needs to be high enough for the number of bins in order to accurately represent the distribution to be demonstrated. The expected variation in a bin can be calculated using the Poisson distribution. If a uniform distribution is assumed over some range, with a certain number of bins, one can determine the number of counts needed in order to reach some desired precision:

$$\lambda = \frac{Nr}{d}, \qquad \sigma = \sqrt{\lambda} \tag{4.1}$$

N	λ	σ	$\frac{\sigma}{\lambda}$
10^4	50	7.07	14%
10^5	500	22.4	4.5%
10^6	5000	70.7	1.4%
10^7	50000	224	0.45%

Table 4.1: Computational uncertainty compared to counts

Where N is the number of counts, r is the range, d is the number of bins, λ is the expected number of counts per bin and σ is the standard deviation per bin assuming a Poisson distribution and large λ. For a relative variation, $\frac{\sigma}{\lambda} = \frac{1}{\sqrt{\lambda}}$. As an example, if one assumes $r = 1$ and $d = 200$, one can see how increasing the number of counts decreases the variation between bins in Table 4.1 and Figure 4.1.

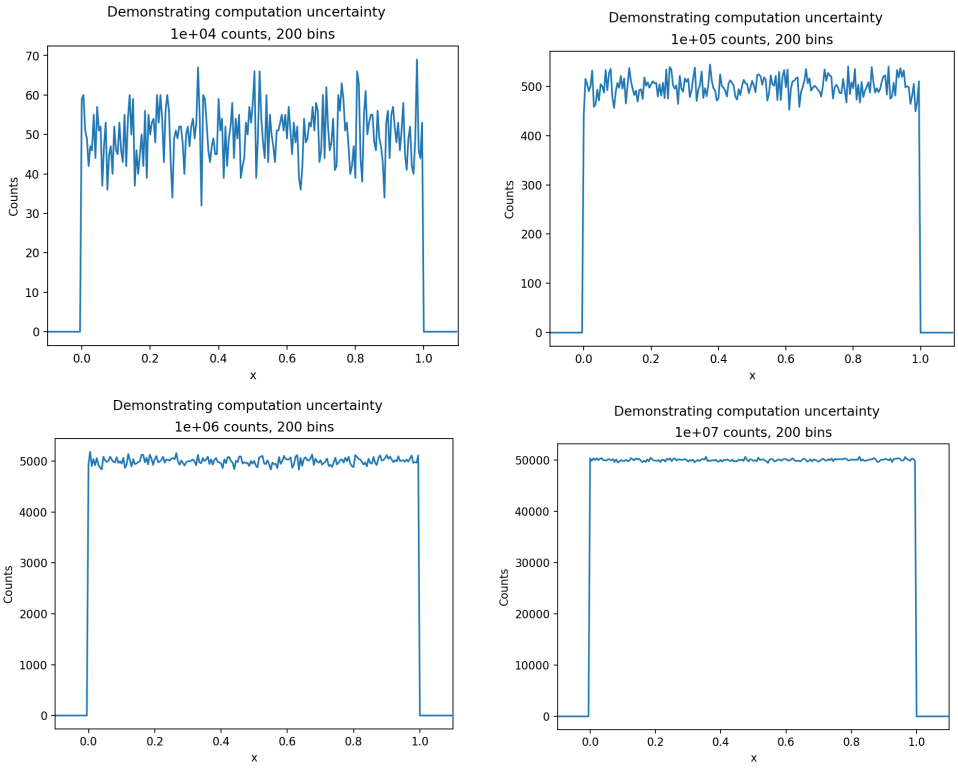

Figure 4.1: The decreasing variation between bins as the number of counts increases.

An increased uncertainty of less than 1% would be desirable, though an increase in counts leads to a longer computation time. For comparison, the full simulation takes approximately 5 minutes for 10^6 counts, making this the most reasonable tradeoff between computation time and computational uncertainty in generating the results for this study.

4.2 Variations in Energy

All effects in the simulation will affect the simulation through either a change in the angles or the energies. There may be shifts (energy loss), randomizations (angular bins), or broadening (energy straggling), each of which will affect the Q-value distribution in a certain way. Here the expected results from variations in energy will be compared to the results from the systematic study of the simulation.

In order to get a first-order approximation of the relationship between Q and the energy, the first derivative can be found, referencing equations A.10, A.11 and A.12 derived in the appendix:

$$\frac{\partial Q}{\partial m_4} = -1, \quad \frac{\partial m_4}{\partial (p_4^2)} = \frac{-1}{2m_4}, \quad \frac{\partial (p_4^2)}{\partial (p_3)} = 2p_3 - 2p_1 cos(\phi),$$

$$\frac{\partial p_3}{\partial E_3} = \frac{E_3}{p_3}, \quad \frac{\partial m_4}{\partial E_4} = \frac{E_4}{m_4}, \quad \frac{\partial E_4}{\partial E_3} = -1, \quad \frac{\partial E_3}{\partial K_3} = 1$$

$$\frac{\partial Q}{\partial K_3} = \frac{\partial Q}{\partial m_4}\left(\frac{\partial m_4}{\partial (p_4^2)}\frac{\partial (p_4^2)}{\partial p_3}\frac{\partial p_3}{\partial E_3}\frac{\partial E_3}{\partial K_3} + \frac{\partial m_4}{\partial E_4}\frac{\partial E_4}{\partial E_3}\frac{\partial E_3}{\partial K_3}\right)$$

$$\frac{\partial Q}{\partial K_3} = (-1)\left(\frac{-1}{2m_4}(2p_3 - 2p_1 cos(\phi))\frac{E_3}{p_3} + \frac{E_4}{m_4}(-1)\right) = \frac{E_3(1 - \frac{p_1}{p_3}cos(\phi)) + E_4}{m_4} \quad (4.2)$$

This equation uses values that can be extracted from the simulation or from the phase space locus. Some numerical examples can be used to deduce the expected distributions for results from the simulation. The values typically used are $m_1 = 7484\,MeV$, $m_2 = 1876\,MeV$, $m_3 = 5603\,MeV$, and $K_1 = 64\,MeV$. For a tetraneutron with a resonance energy of $0\,MeV$, there will be $m_4 = 3759\,MeV$ and $Q = -2.15\,MeV$. All other values are derived from these wherever needed in the following sections using relativistic relationships.

4.2.1 Energy Straggling

One common effect in the simulation is energy straggling. The most general concept is that the initial energy, E_i, will be randomized by some normal distribution with standard deviation σ_E to some energy E_f. The straggling is presumably relatively small, meaning that first order approximations can be used to estimate the resulting distribution. The straggling distribution is given by some Gaussian function:

$$f(\Delta E) \propto \exp(\frac{(\Delta E)^2}{2\sigma_E^2}) \tag{4.3}$$

Transforming to the resulting ΔQ Gaussian:

$$\Delta Q = \tfrac{\partial Q}{\partial E}\Delta E, \qquad f(\Delta Q) \propto \exp(\tfrac{(\Delta Q)^2}{2\sigma_E^2(\frac{\partial Q}{\partial E})^2})$$

$$f(\Delta Q) \propto \exp(\frac{(\Delta Q)^2}{2\sigma_Q^2}), \qquad \sigma_Q = \frac{\partial Q}{\partial E}\sigma_E \tag{4.4}$$

The normalization of the distribution will be a function of the distribution of the energy, which is typically uniform. This process can be applied to several points along

K_3 (MeV)	$\phi(^\circ)$	$\frac{\partial Q}{\partial E}$	$\sigma_Q(MeV)$
12.00	1.75	-1.48	0.14
17.00	18.26	-0.68	0.065
22.00	21.37	-0.24	0.023
27.00	21.93	0.033	0.003
32.00	21.25	0.22	0.021
37.00	19.78	0.36	0.035
42.00	17.65	0.46	0.045
47.00	14.83	0.55	0.053
52.00	11.00	0.61	0.059
57.00	4.21	0.67	0.064

Table 4.2: Samples of Q-value sigma for energy straggling

the locus to demonstrate the variation of the width over different energies. For example, beam energy width is 0.15% at 64 MeV, giving $\sigma_E = 0.096\,MeV$. Corresponding values of σ_Q are shown in Table 4.2.

From this table, it appears there will be a range of more broad and less broad Gaussian distributions in superposition. There is a bias towards the lower values of σ_Q, which means the distributions should be thin with a short, flat base, as opposed to the bell shape of a regular normal distribution. Looking at examples in Chapter 3, effects such as beam energy spread, IC energy straggling and silver foil energy straggling show this shape. It also shows up in the detector resolutions, as a similar effect is applicable with some added complication from σ_E being a function of energy.

4.2.2 Energy Loss Before the Target

The same principle as used in studying energy straggling applies to energy loss, the change in energy can be converted to a first-order approximation of the change

in Q-value. By looking at the shape of the phase space locus, as energy is lost, the points at higher energy move to a locus associated with a lower Q-value, while points at the lower energies move to a locus with a higher Q-value.

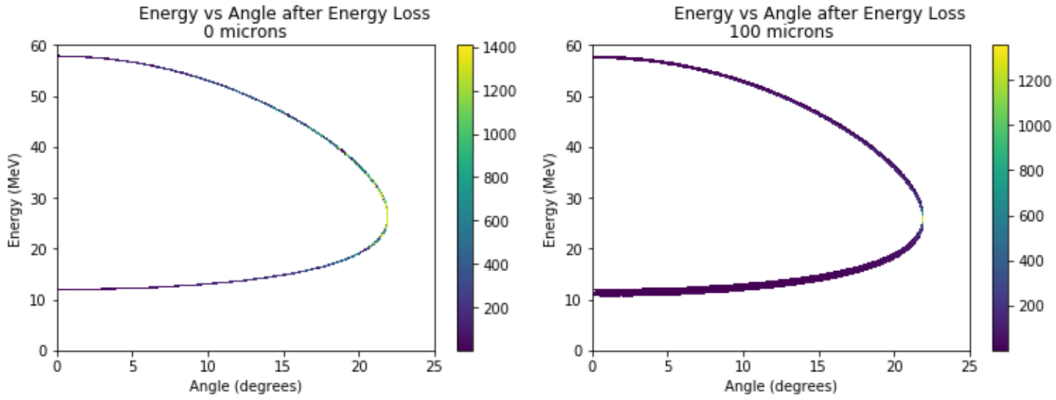

Figure 4.2: The effect of energy loss on the phase space locus

This lines up with the values calculated in section 4.2.1, as the partial derivatives are negative at low energy (energy loss increases Q) and positive at high energy (increases Q) and at the tip of the locus, change in energy moves along the locus, meaning a minimal change in Q.

From Chapter 3, there is a clear difference between energy loss from the material before the target (IC and silver foil) compared to energy loss in the target. The energy loss through the IC and silver foil is applied to each beam event equally, as they are assumed to be almost exactly equal. This is a slight error as there will be minor variations based on the effective angle, energy straggling and energy spread, though these effects are very minimal. As this is practically a variation in beam energy, the Q-value should in fact be insensitive to this effect on its own, as the Q-value is

independent of the beam energy. The variation seen in Q-value is purely an artifact from how the Q-value is defined.

In the Q-value calculations, there is some dependence on beam energy. In the simulation, some standard value of K_1 must be used that is standard for all events, as the energy going into the reaction is not measured for each event. One should therefore define the base K_1 to minimize this change, the ideal such energy being 'the centre of the target'. If one defines K_1 as the incoming beam energy ($64\,MeV$), the energy loss from the IC and silver foil will give some corresponding change to the Q-value, following a similar procedure to what gave equation 4.2:

$$\frac{\partial Q}{\partial E_1} = \frac{\partial Q}{\partial m_4}\left(\frac{\partial m_4}{\partial (p_4^2)}\frac{\partial (p_4^2)}{\partial p_1}\frac{\partial p_1}{\partial E_1} + \frac{\partial m_4}{\partial E_4}\frac{\partial E_4}{\partial E_1}\right)$$

$$\frac{\partial Q}{\partial E_1} = \frac{E_1(1 - \frac{p_3 cos(\phi)}{p_1}) - E_4}{m_4} \tag{4.5}$$

From this, one can find how the corresponding ΔQ will be different for different values of K_3 by using $p_3 cos(\phi) = p_{3x}$ and using the relationship from relativistic boosting to the COM frame (25):

$$E_{3c} = \gamma(E_3 - v_c p_{3x}), \qquad v_c p_{3x} = E_3 - \frac{E_{3c}}{\gamma}$$

$$\frac{\partial p_{3x}}{\partial E_3} = \frac{1}{v_c}, \qquad \frac{\partial^2 Q}{\partial E_1 \partial E_3} = \frac{\partial^2 Q}{\partial E_1 \partial p_{3x}}\frac{\partial p_{3x}}{\partial E_3} = \frac{-E_1}{p_1 m_4 v_c} = \xi \tag{4.6}$$

As this result is independent from the energy K_3, the resulting $\Delta Q = \xi \Delta E_1 \Delta E_3$ is linear with K_3. As we know from the locus, there will be no change in Q at the maximum angle (approximately 21.9°) with an energy of $K_m = 26.3\,MeV$. The

change in Q-value corresponding to a certain K_3 will then be given by:

$$\Delta Q = \xi \Delta E_1 (K_3 - K_m) \tag{4.7}$$

This means that a specific value of K_3 transforms linearly to a value of Q, and as K_3 is evenly distributed coming out of the reaction, an even distribution is seen for the IC energy loss and silver foil energy loss. Changing this reference value of the beam energy to take into account energy loss from the IC (and silver foil, where relevant) will give a value of $\Delta E_1 = E_{ref} - E_1 = 0$, where E_1 has the constant energy loss subtracted for all beam events, which would eliminate this broadening entirely. The reason ΔE_1 is defined this way is that E_{ref} is the value used for E_1 when calculating Q-values in the simulation, meaning that the error introduced into Q comes from how this value varies from the true value of E_1. As this is the 'error' in E_1, the 'error' in Q will change in relation to this.

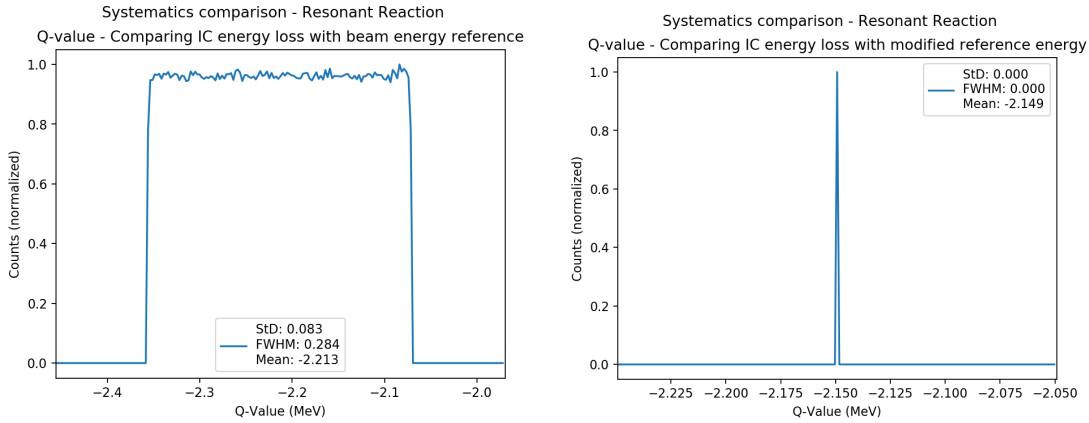

Figure 4.3: IC energy loss with different reference energy before reaction

Using the values referenced previously, and taking the hardcoded value from the simulation of $\Delta E_1 = E_{ref} - E_1 = 0.351\,MeV$, one can get an estimate for ΔQ:

$$E_1 = m_1 + K_1 = 7548\,MeV, \qquad p_1 = \sqrt{E_1^2 - m_1^2} = 980.8\,MeV,$$

$$v_c = \frac{p_1}{K_1+m_1+m_2} = 0.104 \qquad \xi = -0.0197 \qquad \xi\Delta E_1 = -0.00691$$

$$\Delta Q_{max} = (-0.00691)(12.0 - 26.3) = 0.099,\ Q_{max} = -2.15 + 0.099 = -2.05\,MeV$$

$$\Delta Q_{min} = (-0.00691)(57.8 - 26.3) = -0.218,\ Q_{min} = -2.15 - 0.218 = -2.37\,MeV$$

This gives the approximate values seen in the results when using the beam energy as the reference energy.

4.2.3 Energy Loss of ^8He in the Target

The energy loss in the target may not be adjusted for on an event-by-event basis, meaning this is a true inherent broadening effect. There is further complication due to the randomness of which depth in the target the reaction happens. This means that each ^8He and ^6Li will experience a variety of energy losses based on where in the target the reaction happens. At each energy, the energy lost for the specified isotope will range from zero to the amount lost through the entire effective thickness. For ^8He, the effective thickness will just be the depth into the target of the reaction, while for ^6Li it will be based on the angle coming out of the reaction, which will be directly related to the energy.

As ^8He passes through the target with a constant energy of $64\,MeV$ between events in the generated results, and the energy lost is relatively small compared to the total energy, the ^8He energy loss can be modelled as having constant stopping power. Both

the simulation and LISE++ (22) confirm a stopping power of $\frac{dE}{dx} = -0.0018\frac{MeV}{\mu m}$, this can be used as the constant stopping power. Equation 4.5 can be used in this case, as the energy loss will be a change in E_1:

$$E_1 = E_{ref} + Sd, \qquad S = \frac{dE}{dx}, \qquad \Delta E_1 = E_{ref} - (E_{ref} + Sd) = -Sd$$

$$\Delta Q = -\xi Sd(K_3 - K_m) \tag{4.8}$$

Where S is the stopping power and d is the distance through the target. As the distance will be randomized from $0\,\mu m$ to $100\,\mu m$, each value of K_3 will have a corresponding range of Q-values.

To interpret how this will appear as a histogram, the distribution can be considered for a single distance. The energy K_3 is assumed to be uniformly distributed, and the ΔQ distribution for an individual value of d will also be uniformly distributed. Comparing the distributions for different values of d, higher values corresponding to higher ΔQ will cover a broader range. As the distribution in d is assumed to be uniform, a larger range of ΔQ will spread the distribution thinner compared to a small range. The shape a histogram will take is each of these distributions added on top of each other, with the short, broad shape on the bottom, moving up towards tall, thin shapes on the top. This leads to a wide base curving up to a thin peak.

This method has been used in Figure 4.4 to replicated the histogram seen for ^8He energy loss in the target. As a first order approximation, it lines up well. The expected maximum and minimum values can be approximated using the same method as used for energy loss before the target. The maximum ΔQ will be at the maximum distance,

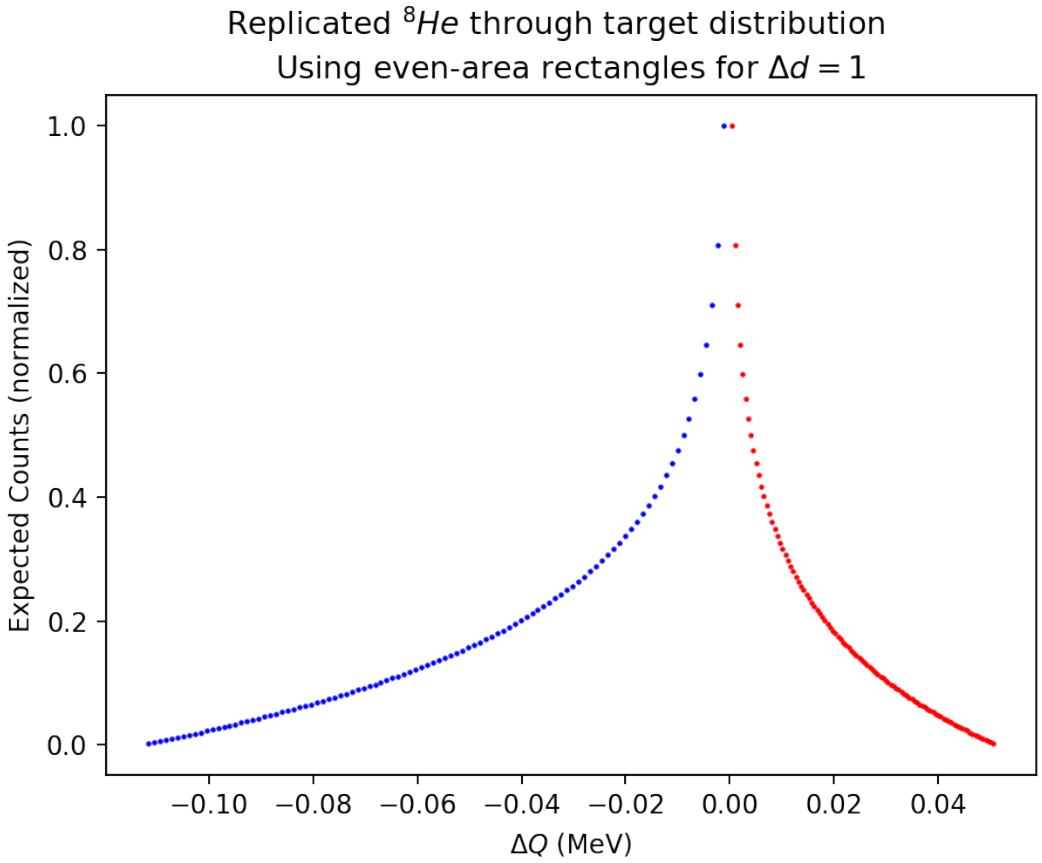

Figure 4.4: Expected histogram distribution with $\Delta d = 1$

$d = 100\,\mu m$, going from the minimum value of Q at the highest K_3 of $57.8\,MeV$ to the highest value at the lowest K_3 at $12.0\,MeV$.

$$\xi = -0.0197, \qquad S = -0.0018, \qquad d = 100, \qquad \Delta Q = -\xi S d(K_3 - K_m)$$

$$\Delta Q_{max} = -(-0.0197)(-0.0018)(100)(12.0 - 26.3) = 0.0507\,MeV,$$

$$\Delta Q_{min} = -(-0.0197)(-0.0018)(100)(57.8 - 26.3) = -0.112\,MeV$$

$$Q_{max} = -2.15 + 0.0507 = -2.10\,MeV, \qquad Q_{min} = -2.15 - 0.112 = -2.26\,MeV$$

The values of the highest broadening line up, and the distribution of the histogram takes the expected shape, meaning that the energy loss for ^8He in the target appears as expected.

4.2.4 Energy Loss of ^6Li in the Target

When calculating the energy loss for ^6Li in the target, there are a few more considerations to take into account. The energy loss can not be assumed to be constant, as there will be a broader range of energies. Furthermore, as the angles reach up to approximately 20°, there will be a slightly increased effective width at these angles meaning more energy loss.

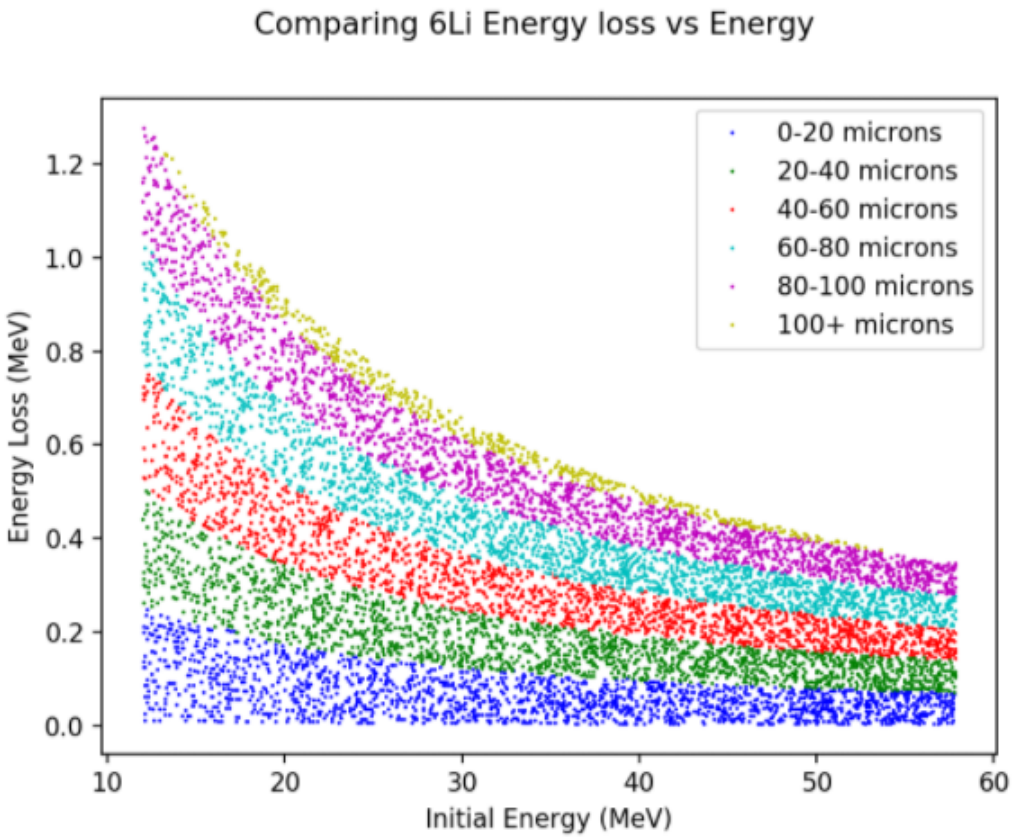

Figure 4.5: Energy loss of ^6Li in the target

Using equation 4.2, an approximation for ΔQ for the maximum distance at each energy can be calculated. Using the same method as for ^8He, the distance can then be assumed to be uniformly distributed and the histogram can be replicated. Using

K_3 (MeV)	$\phi(^\circ)$	ΔK_3	$\frac{\partial Q}{\partial K_3}$	$\Delta Q(MeV)$	$\lvert\frac{1}{\Delta Q}\rvert$	(x, y)
12.0	1.14	-1.30	-1.49	1.93	0.518	(1.93, 0.518)
17.0	18.27	-1.04	-0.681	0.709	1.41	(0.709, 1.93)
22.0	21.40	-0.862	-0.243	0.210	4.77	(0.210, 6.70)
27.0	21.97	-0.718	0.032	-0.023	42.9	(-0.023, 72.5)
32.0	21.30	-0.622	0.222	-0.138	7.25	(-0.138, 29.6)
37.0	19.82	-0.544	0.360	-0.196	5.11	(-0.196, 22.3)
42.0	17.70	-0.479	0.465	-0.223	4.49	(-0.223, 17.2)
47.0	14.88	-0.430	0.547	-0.235	4.25	(-0.235, 12.7)
57.0	4.22	-0.352	0.669	-0.235	4.25	(-0.235, 8.44)
52.0	11.04	-0.389	0.614	-0.239	4.19	(-0.239, 4.19)

Table 4.3: Approximating Q-value histogram from ^6Li energy loss in target

LISE++ (22) to find energy losses, the values can be calculated and the corresponding points on the replicated histogram can be plotted. The ordering goes back on the largest ΔQ, hence the slight reordering:

This gives some idea as to how the histogram should appear. There is some minimum value of ΔQ at an energy slightly below the maximum, as the energy loss decreases at a greater rate than $\frac{\partial Q}{\partial K_3}$ increases. This leads to several energies where ΔQ is changing very slowly, and as a result gives a high slope. This can be seen in the (x, y) points, where there is very little change in x but a large increases in y. While these points were plotted manually with reference to LISE++, as they agree with the predicted energy loss given by the simulation, the function from the simulation can be used to calculate energy loss for more points and plot the distributions with a larger number of points:

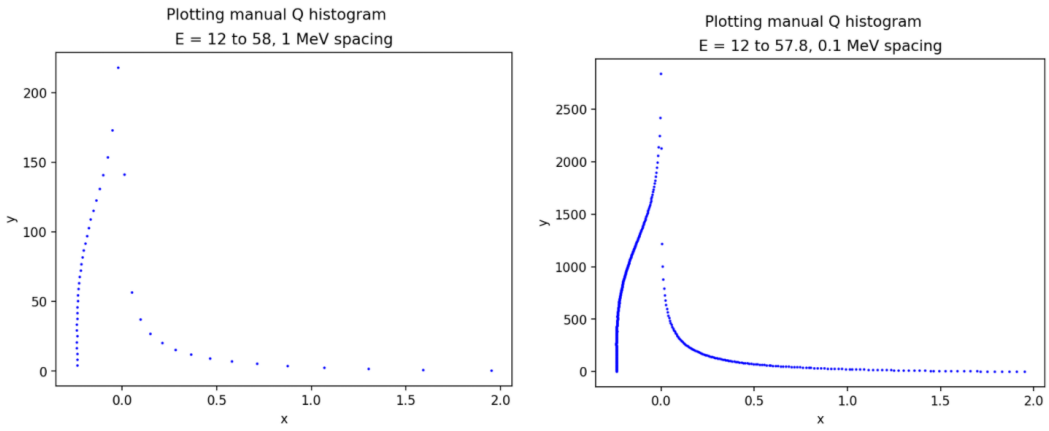

Figure 4.6: Replicated $6Li$ histogram with more points

These plots replicate the histogram for $6Li$ energy loss in the target from the simulation.

4.3 Variations in Angle

Much like in the case of energy, the expected effect of variation in the angle can be studied to compare to the generated results. These effects show up at angular straggling, bin randomization and detector geometry cuts. The first-order relationship between Q and ϕ will be here, as it was with K_3:

$$\frac{\partial Q}{\partial \phi} = \frac{\partial Q}{\partial m_4}\frac{\partial m_4}{\partial (p_4^2)}\frac{\partial (p_4^2)}{\partial cos(\phi)}\frac{\partial cos(\phi)}{\partial \phi} = (-1)(\frac{-1}{2m_4})(-2p_1p_3)(-sin(\phi))$$

$$\frac{\partial Q}{\partial \phi} = \frac{p_1 p_3 sin(\phi)}{m_4} \tag{4.9}$$

4.3.1 Angular Straggling

Following the same procedure as for energy straggling, angular straggling can be modelled as a Gaussian distribution. The effect from the straggling itself is not in

the angle from the reaction, which itself will be unchanged, but in the angle going into or coming out of the target. All angular straggling effects are before the target a distance d or in the target at $d = 0$, with detectors a distance l from the target, as demonstrated in Figure 4.7. With a change in angle of θ_e, the particle will enter the target at a different position, Δy_e, and come out at an angle $\phi + \theta_e$. As measured from the centre of the target, the resulting angle measured on the detector will be ϕ_m.

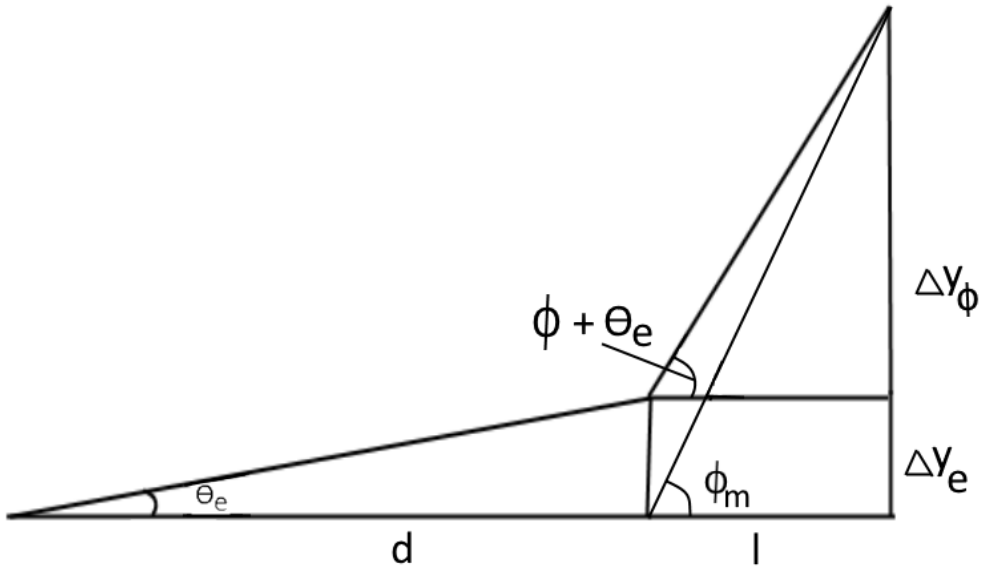

Figure 4.7: Effect of angle broadening on measured angle

Finding ϕ_m for a given θ_e, using a small angle approximation for θ_e:

$$\Delta y_e = d\,tan(\theta_e) \simeq d\,\theta_e, \qquad \Delta y_\phi = l\,tan(\phi + \theta_e)$$

$$tan(\phi + \theta_e) \simeq tan(\phi) + \tfrac{dtan(\phi)}{d\phi}\theta_e = tan(\phi) + sec^2(\phi)\,\theta_e$$

$$tan(\phi_m) = \frac{l\,tan(\phi) + (d + l\,sec^2(\phi))\theta_e}{l} = tan(\phi) + (\frac{d}{l} + sec^2(\phi))\,\theta_e \qquad (4.10)$$

This can be related to the Q-value through Equation 4.9:

$$\frac{\partial Q}{\partial \theta_e} = \frac{\partial Q}{\partial \phi_m}\frac{\partial \phi_m}{\partial \theta_e}, \qquad \frac{\partial tan(\phi_m)}{\partial \theta_e} = \frac{\partial tan(\phi_m)}{\partial \phi_m}\frac{\partial \phi_m}{\partial \theta_e}, \qquad \frac{\partial \phi_m}{\partial \theta_e} = cos^2(\phi_m)\frac{\partial tan(\phi_m)}{\partial \theta_e}$$

$$\frac{\partial Q}{\partial \theta_e} = \frac{p_1 p_3 sin(\phi)}{m_4} cos^2(\phi)(\frac{d}{l} + sec^2(\phi)) = \frac{p_1 p_3 sin(\phi)}{m_4}(1 + \frac{d}{l}cos^2(\phi)) \tag{4.11}$$

With the approximation that $\phi_m \simeq \phi$, which is true when θ_e is small, as has been assumed. When the broadening happens in the target, this reduces to 4.9 as $\frac{d}{l} \simeq 0$, which is to be expected as the only effect comes from the change of the measured ϕ, with no contribution from the change in position. ($\Delta y_e = 0$) The exact same procedure used for energy straggling can be used assuming a Gaussian distribution in θ_e with standard deviation σ_θ:

$$f(\Delta Q) \propto \exp(\frac{(\Delta Q)^2}{2\sigma_Q^2}), \qquad \sigma_Q = \frac{\partial Q}{\partial \theta_e}\sigma_\theta \tag{4.12}$$

In the case of IC angular straggling, there is a hardcoded standard deviation of $\sigma_\theta = 0.869\, mrad$ with $d = 52\, cm$ and $l = 25\, cm$. Using the other standard values for the relevant variables, the values of σ_Q can be calculated over the range of energies, as demonstrated in Table 4.4.

As with energy straggling, this distribution will be the superposition of many Gaussian distributions each with σ_Q. Unlike in the case of energy straggling, the broadening here is more consistent through the different energies. This gives a peak with a more evenly distributed width.

K_3 (MeV)	$\phi(^\circ)$	$\frac{\partial Q}{\partial \theta_e}$	$\sigma_Q(MeV)$
12.00	1.75	8.49	0.0074
17.00	18.26	102.8	0.0893
22.00	21.37	132.6	0.115
27.00	21.93	149.8	0.130
32.00	21.25	159.2	0.138
37.00	19.78	161.9	0.141
42.00	17.65	157.1	0.137
47.00	14.83	143.1	0.124
52.00	11.00	114.6	0.0996
57.00	4.21	47.01	0.0410

Table 4.4: Samples of Q-value sigma for angular straggling

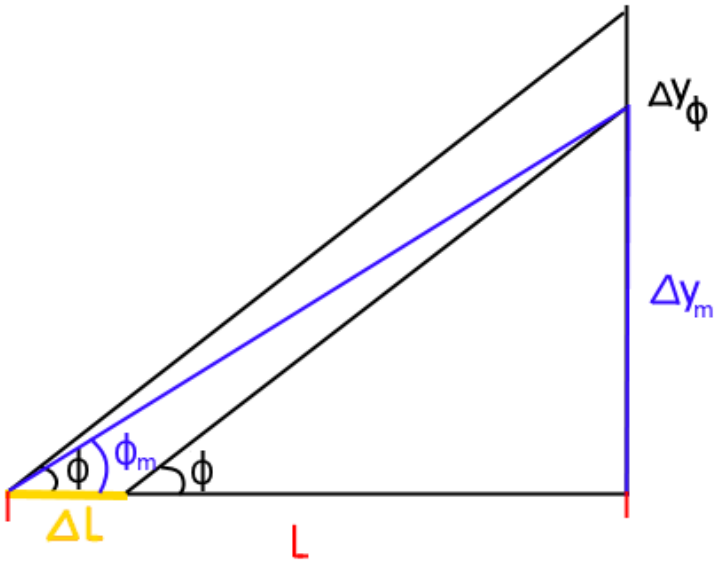

Figure 4.8: Effect of target angle broadening on measured angle

4.3.2 Angle Broadening from Target

The thickness of the target will give a very small variation in the angle into the detector based on the distance through the target the reaction happens. Much like in the case of the energy loss before the target, there must be some baseline position in the target to measure l from in Figure 4.8:

$$\Delta y_m = (l - \Delta l)\, tan(\phi), \qquad tan(\phi_m) = \tfrac{\Delta y_m}{l} = (1 - \tfrac{\Delta l}{l})\, tan(\phi)$$

$$\frac{\partial Q}{\partial \Delta l} = \frac{\partial Q}{\partial \phi_m}\frac{\partial \phi_m}{\partial \Delta l} = \frac{p_1 p_3 sin(\phi)}{m_4} cos^2(\phi)(\frac{-tan(\phi)}{l}) = \frac{-p_1 p_3 sin^2(\phi) cos(\phi)}{m_4 l} \tag{4.13}$$

This will be highest at the highest angle, 21.9°, with energy 26.3 MeV. The maximum value of ΔQ from this effect can be calculated with $l = 25\,cm$ and $\Delta l = 100\,\mu m$:

$$\Delta Q = \tfrac{\partial Q}{\partial \Delta l}\Delta l = \tfrac{-(980.8)(543.5)(0.129)}{(3758)}\tfrac{100\,\mu m}{25\,cm} = 0.00732\,MeV$$

This gives a very small variation in Q, on the same order as seen in the results, which show a FWHM of 0.003. This FWHM also approximately half of the maximum calculated here, as would be expected from a roughly linear relationship given by this approximation.

4.3.3 Angular Segmentation

The detector is divided into angular segments, with the angle measurements only able to be measured to within one of these. In the simulation, if an angle is inside the bin, then it is randomized to somewhere in that bin. This causes broadening of the Q-value, as the randomization will given a combination of energy and angle associated with a different reaction Q-value. Along with this, there will be cuts due to the detector geometry, as the smallest angles are not covered by the detector.

The angular bins can be found from the geometry of the detector, which has an inner radius of $r_i = 5\,cm$ and an outer radius of $r_o = 13\,cm$ with $\Delta r = 0.5\,cm$ segments across the ring, located $d = 25\,cm$ from the target. These result in 16 segments, each of which with an inner and outer angle. The corresponding angle ranges can be

calculated, each with two energy ranges for all except the highest angle bin in the phase space, where they merge. The angles covered by the detector go higher than the angles in the phase space, so for this analysis only those in the standard resonant reaction phase space are of interest.

$$\phi_n = tan^{-1}(\frac{r_i + n\Delta r}{d}) \tag{4.14}$$

$$\phi_0 = tan^{-1}(\tfrac{5}{25}) = 11.3°, \qquad \phi_{11} = tan^{-1}(\tfrac{10.5}{25}) = 22.8°, \qquad \phi_{max} = 21.9°$$

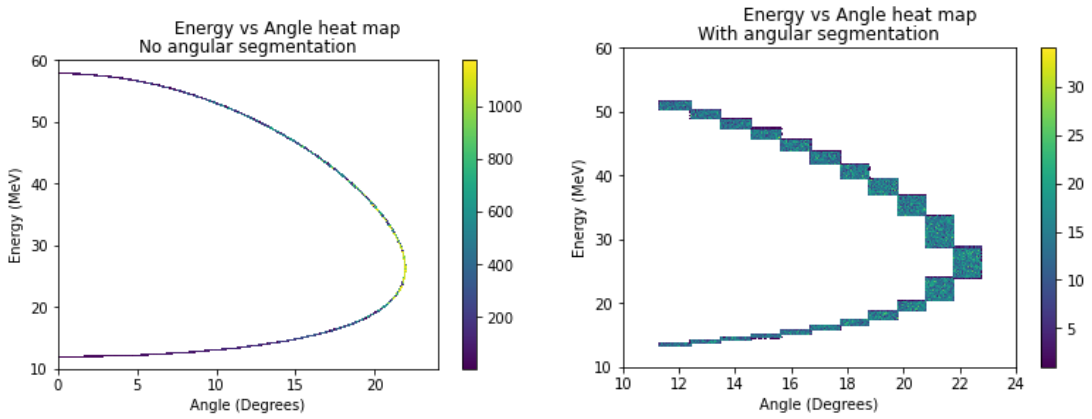

Figure 4.9: The phase space locus comparing segmentation

In each bin, as both angle and energy are assumed to be evenly distributed, the points will be evenly distributed throughout the bin. The unrandomized locus passes through two corners of every bin, meaning that these corners will have no deviations in Q-value. The other two corners will have minima and maxima of ΔQ, with those corners closer to the 'centre' of the locus with a lower Q-value, and those away from the 'centre' with a higher Q-value. The highest bin, in which the maximum value of ϕ is found, the two corners have higher Q-values.

n	ϕ (Degrees)	θ_1 (Degrees)	E_1 (MeV)	θ_2 (Degrees)	E_2 (MeV)
0	11.31	52.88	48.60	143.56	15.00
1	12.41	56.12	47.58	141.13	15.57
2	13.50	59.37	46.54	138.66	16.20
3	14.57	62.65	45.46	136.12	16.90
4	15.64	66.02	44.33	133.47	17.69
5	16.70	69.50	43.12	130.68	18.57
6	17.74	73.19	41.81	127.66	19.59
7	18.78	77.16	40.35	124.33	20.80
8	19.80	81.63	38.64	120.50	22.26
9	20.81	87.04	36.48	115.70	24.20
10	21.80	95.42	32.97	107.92	27.52
11	22.78	—	—	—	—

Table 4.5: Angles at detector segments and corresponding kinematics for resonant reaction

As a crude first-order approximation, for the segments where the locus passes through opposite corners, the path it takes can be assumed to be linear. Every other locus passing through will cover some slightly shorter path. As the area can be assumed to be made up of many of those paths, with each having a corresponding fraction of the evenly-spaced counts, the distributions of Q-values will correspond to the relative lengths. For example, in Figure 4.3.3, the blue line will correspond to the regular resonant reaction with $Q = -2.15\,MeV$ while the red lines correspond to equally likely values greater than and less than that value. Each path can be parameterized by a variable λ going from 0 to 1, as shown in the figure.

The lengths are given based on points and corresponding distances in the figure:

$$(\phi_2 - \Delta\phi\lambda, E_2) \rightarrow (\phi_2, E_2 - \Delta E\lambda)$$

$$s = \sqrt{(\phi_2 - \Delta\phi\lambda - \phi_2)^2 + (E_2 - (E_2 - \Delta E\lambda))^2}$$

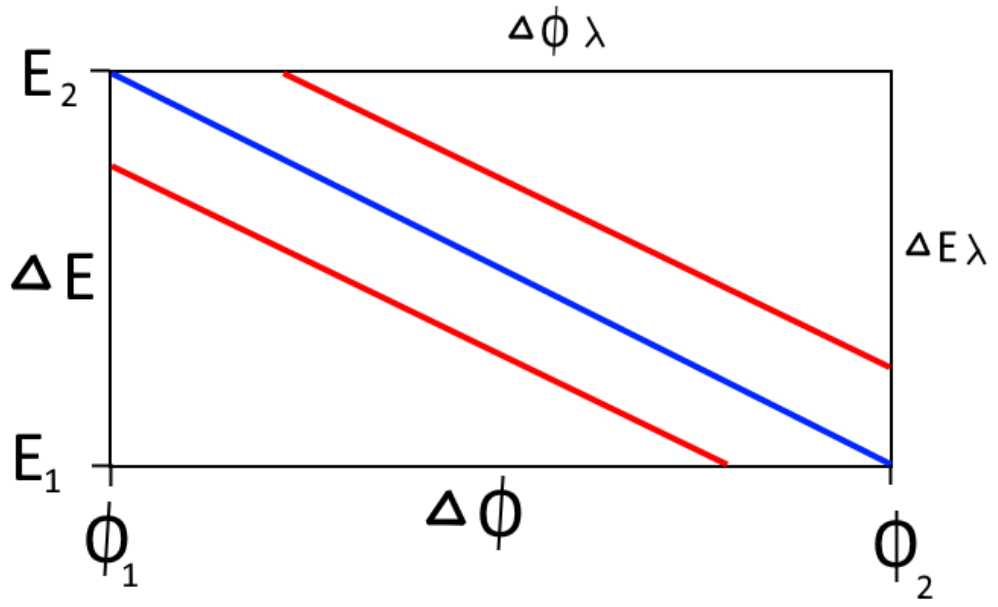

Figure 4.10: A simplified model of the Q-value loci through randomized segments

$$s = \sqrt{(-\Delta\phi\lambda)^2 + (\Delta E\lambda)^2} = \sqrt{\Delta\phi^2 + \Delta E^2}\lambda$$

Given that the distance is proportional to the parameter λ, the distribution will be linear on each side, with the most likely value at the resonant reaction Q-value. This gives roughly triangular distributions, each with a number of counts proportional to the energy range covered, with widths dependent on the maximal variation in Q-value for that segment. The one exception is the maximal angle bin, which is a much more complicated case. A simple understanding can be seen from the fact that while the minimum angle value of the bin is 21.8° and the maximum value is 22.8°, the maximum angle from the locus is 21.9°. For an equal energy, a higher value of ϕ gives a higher value of Q, as seen in equation 4.9. Therefore, as the randomizations will generally increase the angle, one should expect this segment to contribute more towards a higher number of Q-value counts than the resonant reaction value.

For the angular segmentation, the prediction of a triangular distribution with a slight asymmetry towards higher Q-values lines up with the result from the simulation. The effect of the detector geometry on the distribution is more indirect. It will not show up directly in a the resonant distribution, as it simply removes certain counts, though it does cut off lower Q-values of the non-resonant distribution and may modify certain distributions studied where lower angles contribute to broadening.

Chapter 5

Conclusion

An experiment was carried out to study the reaction $^{8}He(d,^{6}Li)4n$ at the IRIS facility at TRIUMF in Vancouver, BC. In order to understand the sensitivity of the IRIS setup to resonant tetraneutron events compared to the non-resonant four-neutron breakup, a simulation was developed. A systematic study showed that the results of the simulation are consistent with what would be expected from the physics of the setup. The final combined results of the simulation for the resonant and non-resonant reaction can be compared to determine the sensitivity of the experiment.

Running the simulation for both the resonant and non-resonant reaction shows their distributions. With the full simulation with no resonance energy or width, there is a clear distinction between the two peaks with minimal overlap, as shown in Figure 5.1. The true sensitivity, however, depends on the exact Q-value and the relative cross-sections of the resonant and non-resonant reaction. In the region where the two distributions overlap, the ability to distinguish whether a count in this region would come from either distribution is diminished. Even without knowing anything about the cross-sections, some statements about the sensitivity can still be made.

Taking into account the resonance energy, the resonant peak would be shifted to a lower Q-value towards the non-resonant distribution. As resonance energy is the

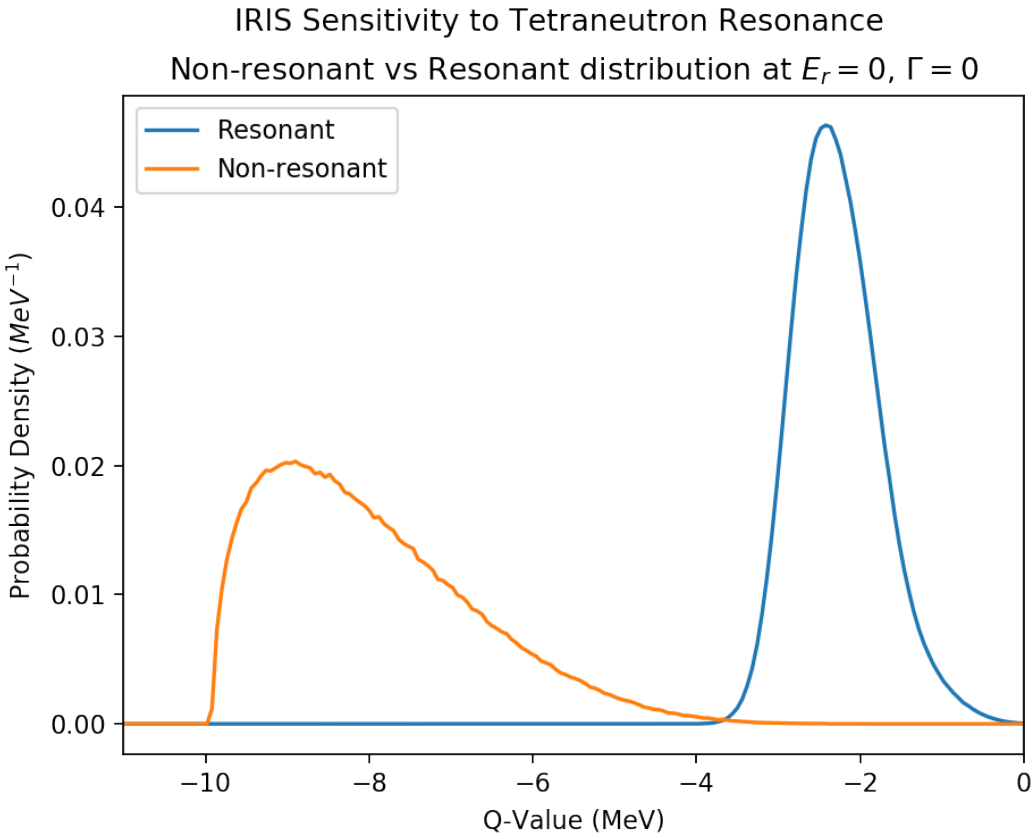

Figure 5.1: The missing mass spectrum for resonant and non-resonant reactions

excitation energy of the tetraneutron resonance, it increases the mass and as a result gives a lower Q-value. As a result, the higher the resonance energy, the more indistinguishable the resonant distribution becomes from the non-resonant distribution. With an increased resonance width, there will be even more overlap with the non-resonant peak, but also the potential for more counts that are at a higher Q-value that do not overlap with the non-resonant distribution. The resonance width is assumed to be given by a Breit-Wigner distribution:

$$P(M) = \frac{\Gamma}{2\pi[(M - M_0)^2 + (\frac{\Gamma}{2})^2]} \tag{5.1}$$

Where Γ is the width, M_0 is the mass of the tetraneutron resonance, taking into account resonance energy E_r, and P_M is the probability density function. Using the same value for E_r as measured at RIKEN of $0.83\,MeV$ and using the upper bound given by this experiment of $\Gamma = 2.6\,MeV$, the sensitivity of the experiment to such an experiment can be seen in Figure 5.2. While the experiment is now less sensitive to the resonant tetraneutron signature, there are still a region of the missing mass spectrum where a resonant tetraneutron event would be distinguishable from a non-resonant event.

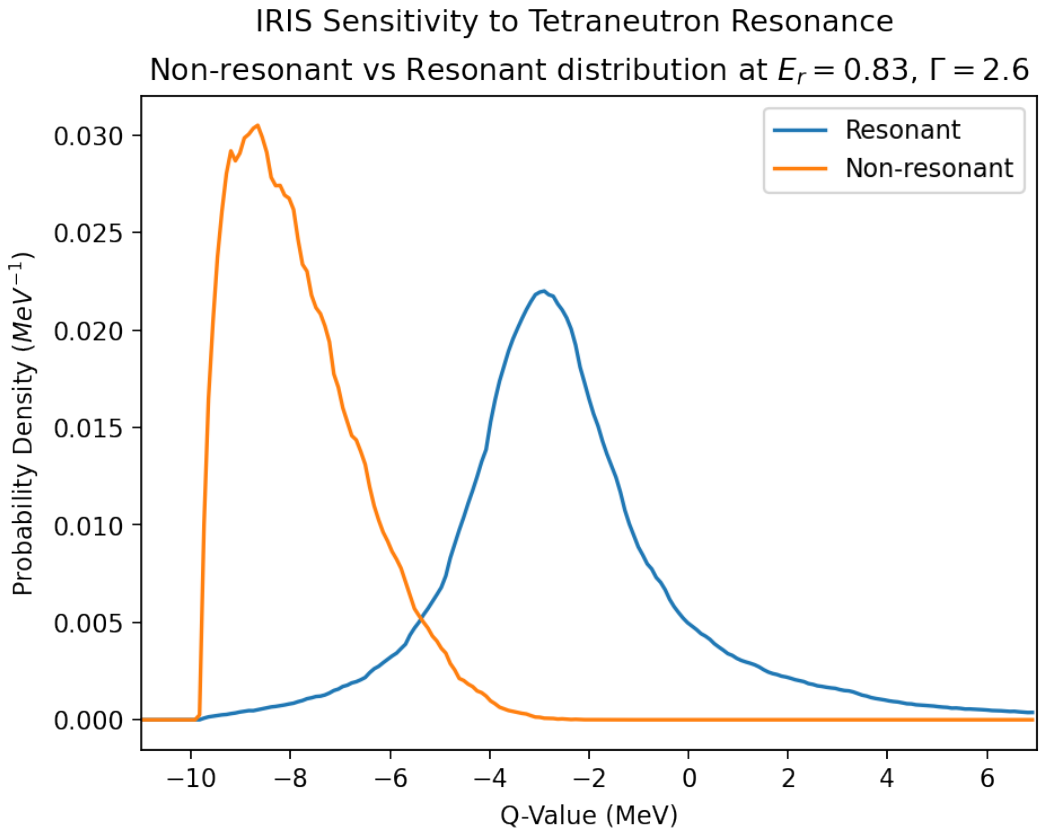

Figure 5.2: The missing mass spectrum taking into account E_r and Γ

In contrast to the GANIL experiment, this experiment would be measuring the missing mass spectrum, which means that these counts could be directly related to a resonant tetraneutron, not just the potential of an increased correlation between the neutrons. In contrast to the RIKEN experiment, events with higher Q-value not accounted for by the non-resonant distribution could only be accounted for by the resonant distribution, no other background such as ^{8}He breakup. In contrast to the GANIL-SPIRAL experiment, the target is entirely deuterium, so this too will give no background in the resonant reaction region.

Given the kinematics of the resonant and non-resonant reaction and the physical effects from the IRIS setup, an experiment to search for the signature of a tetraneutron resonance with this setup would be able to distinguish such a resonance. There is a significant likelihood that an event that could be attributed to a resonant tetraneutron would have a low chance of being attributed to any other source compared to previous experiments. As a result, this experiment provides the sensitivity in measuring the missing mass spectrum of this reaction that would be required to distinguish the signature of a tetraneutron resonance.

Appendix A

Kinematics Calculations

The kinematics of reactions are important in several aspects of this work. Here, the derivation of laboratory quantities and the conversion between Q-value and laboratory energies and angles for two-body reactions is covered. The convention here will follow Figure 2.2, with the particles 1-4 as labelled, m as the mass, E as the total relativistic energy, K as the kinetic energy and p as the momentum. Angle ϕ and λ refer to the laboratory frame angles of particles 3 and 4 respectively. All calculations in this section assume a two-body reaction, though may be applied to many-body reactions, such as described for the missing mass method in subsection 2.1.2. All analysis shown is done relativistically to allow it to be applied to a broad range of reactions, with $c = 1$.

A.1 Finding Laboratory Energies and Angles

First, assuming a given reaction, the energies and angles in the laboratory frame can be found from principles of energy and momentum conservation. For this calculation, the first step is conversion to the COM frame. As this frame is defined as having zero momentum, to convert from the laboratory frame where particle 1 has momentum in the positive-x direction and particle 2 is stationary, the system is boosted into a new inertial frame using relativistic transformations (25) characterized by a negative-x

velocity v_c:

$$p_{1c} = \gamma(p_1 - E_1 v_c) \qquad p_{2c} = \gamma(p_2 - E_2 v_c)$$

$$p_{1c} = -p_{2c}, \qquad p_1 - E_1 v_c = m_2 v_c$$

$$v_c = \frac{p_1}{K_1 + m_1 + m_2} \tag{A.1}$$

$$E_{1c} = \frac{E_1 - p_1 v_c}{\sqrt{1 - v_c^2}} \qquad E_{2c} = \frac{m_2}{\sqrt{1 - v_c^2}} \tag{A.2}$$

Given conservation of energy and momentum, the properties of particle 3 and 4 in the COM frame can be derived. The only free variable in the COM frame will be the angle θ as seen in Figure 2.2 a).

$$E_{Tot} = E_{1c} + E_{2c} = E_{3c} + E_{4c} \qquad p_{3c} = p_{4c} = p_c$$

$$E_{Tot} = \sqrt{p_c^2 + m_3^2} + \sqrt{p_c^2 + m_4^2} \tag{A.3}$$

This equation can be solved for p_c:

$$p_c = \frac{1}{2E_{Tot}} \sqrt{(E_{Tot} - m_3 - m_4)(E_{Tot} + m_3 - m_4)(E_{Tot} - m_3 + m_4)(E_{Tot} + m_3 + m_4)} \tag{A.4}$$

With this expression, the components of the momenta can be found and transformed back into the laboratory frame:

$$p_{cx} = p_c \, cos(\theta) \qquad p_{cy} = p_c \, sin(\theta)$$

$$p_{3x} = \frac{p_{cx} + E_{3c} v_c}{\sqrt{1 - v_c^2}}, \qquad p_{3y} = p_{cy} \tag{A.5}$$

$$p_{4x} = \frac{-p_{cx} + E_{4c} v_c}{\sqrt{1 - v_c^2}}, \qquad p_{4y} = -p_{cy} \tag{A.6}$$

$$\phi = tan^{-1}(\frac{p_{3y}}{p_{3x}}), \qquad \lambda = tan^{-1}(\frac{p_{4y}}{p_{4x}}) \tag{A.7}$$

$$p_3 = \sqrt{p_{3x}^2 + p_{3y}^2}, \qquad E_3 = \sqrt{p_3^2 + m_3^2}, \qquad K_3 = E_3 - m_3 \tag{A.8}$$

$$p_4 = \sqrt{p_{4x}^2 + p_{4y}^2}, \qquad E_4 = \sqrt{p_4^2 + m_4^2}, \qquad K_4 = E_4 - m_4 \tag{A.9}$$

From this calculation, all energies and angles of the products in the laboratory frame are found, parameterized by the free variable θ. The lighter product will cover all angles from 0° to 180°, while the more massive product will have some locus through phase space with a parabolic shape. As a result, each angle will correspond to two energies, with the highest and lowest energies corresponding to 0°. There will be some maximum angle where increasing energy begins to decrease the angle. This means that the heavy product will be restricted to small angles, while the light product is unrestricted in angle.

A.2 Finding Q from K_3 and ϕ

As seen in section A.1, the properties of reaction products in the laboratory can be derived precisely with only one free variable. Each locus derived in this process corresponds to a specific Q-value, derived from the masses of the reactants and products. This is described in more detail in the section on the missing mass method. The process for finding the Q-value from a given value of K_3 and ϕ is given using the following equations:

$$E_4 = E_1 + E_2 - E_3, \qquad Q = m_1 + m_2 - m_3 - m_4 \tag{A.10}$$

$$p_{4x} = p_1 - p_3 cos(\phi), \qquad p_{4y} = -p_3 sin(\phi)$$

$$p_4^2 = (p_1 - p_3 cos(\phi))^2 + p_3^2 sin^2(\phi) = p_1^2 + p_3^2 - 2p_1 p_3 cos(\phi) \tag{A.11}$$

$$m_4 = \sqrt{E_4^2 - p_4^2} \tag{A.12}$$

The results from equation A.12 can be used in equation A.10 to get the Q-value. As m_4 is not assumed, there is no requirement that the reaction is truly a 2-body reaction, this is simply the Q-value if it were a 2-body reaction.

Bibliography

[1] Hansen, P. G. *Nuclear Structure at the Drip Lines*. Hyperfine Interactions, vol. 43, no. 1-4, Dec. 1988, pp. 379–394

[2] Hoyle, F. *On Nuclear Reactions Occuring in Very Hot STARS .I. The Synthesis of Elements from Carbon to Nickel*. The Astrophysical Journal Supplement Series, vol. 1, Sept. 1954, p. 121

[3] Kezerashvili, Roman Ya. *A Short Summary on the Search of Trineutron and Tetraneutron*. Fission and Properties of Neutron-Rich Nuclei, 3 Oct. 2017

[4] Pieper, Steven C. *Can Modern Nuclear Hamiltonians Tolerate a Bound Tetraneutron?*. Physical Review Letters, vol. 90, no. 25, 27 June 2003

[5] Hiyama, E., et al. *Possibility of Generating a 4-Neutron Resonance with a T=3/2 isospin 3-Neutron Force*. Physical Review C, vol. 93, no. 4, 29 Apr. 2016

[6] Shirokov, A.M., et al. *Prediction for a Four-Neutron Resonance*. Physical Review Letters, vol. 117, no. 18, 28 Oct. 2016

[7] Ivanytskyi, O., et al. *Tetraneutron Condensation in Neutron Rich Matter*. The European Physical Journal A, vol. 55, no. 10, Oct. 2019

[8] Tilley, D.R., et al. *Energy Levels of Light Nuclei a = 4*. Nuclear Physics A, vol. 541, no. 1, May 1992, pp. 1–104

[9] Aleksandrov, D. V., et al. *Search for Resonances in the Three-and Four-Neutron Systems in the 7Li(7Li, 11C)3n and 7Li(7Li, 10C)4n Reactions*. Journal of Experimental and Theoretical Physics Letters, vol. 81, no. 2, Jan. 2005, pp. 43–46

[10] Marqués, F. M., et al. *Detection of Neutron Clusters*. Physical Review C, vol. 65, no. 4, 1 Apr. 2002

[11] Sherrill, B. M., and C. A. Bertulani. *Proton-Tetraneutron Elastic Scattering*. Physical Review C, vol. 69, no. 2, 24 Feb. 2004

[12] Marqués, F. M., et al. *On the Possible Detection of 4n Events in the Breakup of 14Be*. ResearchGate, 6 May 2005

[13] Kisamori, K., et al. *Candidate Resonant Tetraneutron State Populated by TheHe4(He8,Be8)Reaction*. Physical Review Letters, vol. 116, no. 5, 3 Feb. 2016

[14] Fortier, S., et al. *Search for Resonances in 4n, 7H and 9He via Transfer Reactions*. AIP Conference Proceedings, 2007

[15] Barrett, Bruce R., et al. *Ab Initio No Core Shell Model*. Progress in Particle and Nuclear Physics, vol. 69, Mar. 2013, pp. 131–181

[16] Rene Brun and Fons Rademakers *ROOT - An Object Oriented Data Analysis Framework*. Proceedings AIHENP'96 Workshop, Lausanne, Sep. 1996, Nucl. Inst. Meth. in Phys. Res. A 389 (1997) 81-86.

[17] Harris, C. R., et al. *Array programming with NumPy*. Nature 585, 357–362, 2020

[18] James, F. *Monte-Carlo phase space*. CERN-68-15, May 1968

[19] Rutherford, Ernest et al. *The Scattering of alpha and beta Particles*. Radiations from Radioactive Substances, Apr. 1911, pp. 191–239

[20] Bethe, H. A. *Molières Theory of Multiple Scattering*. Physical Review, vol. 89, 1953, pp. 1256-1266

[21] Highland, Virgil L. *Some practical remarks on multiple scattering*. Nuclear Instruments and Methods, vol. 129, 22 Aug. 1975, pp. 497–499

[22] Tarasov, O.B., and D. Bazin *LISE++: Radioactive Beam Production with in-Flight Separators*. Nuclear Instruments and Methods in Physics Research Section B: Beam Interactions with Materials and Atoms, vol. 266, no. 19-20, 2008, pp. 4657–4664.

[23] Virtanen, P. et al. *SciPy 1.0: Fundamental Algorithms for Scientific Computing in Python*. Nature Methods, 17(3), 261-272, 2020

[24] Kumar, Sunil, and P.K. Diwan *Energy loss and straggling of -particles in Ag and Sn metallic foils*. Journal of Radiation Research and Applied Sciences, vol. 8, no. 4, 2015, pp. 538–543

[25] Walet, N. *Lorentz Transformations of Energy and Momentum.*. https://chem.libretexts.org/@go/page/15052, 13 Aug. 2020